Aerospace Engineering Sciences Graduate Theses & Dissertations

Aerospace Engineering Sciences

Spring 1-1-2017

Study of the Unsteady Aerodynamics Associated with a Cycloidally Rotating Blade

Nishant Agarwal
University of Colorado at Boulder, nishant.agarwal@colorado.edu

Study of the Unsteady Aerodynamics associated with a Cycloidally Rotating Blade

by

Nishant Agarwal

B.Tech., Mech. Eng., G.B.P.E.C, 2012

A thesis submitted to the

Faculty of the Graduate School of the

University of Colorado in partial fulfillment

of the requirements for the degree of

Master of Science

Ann and H.J. Smead Department of Aerospace Engineering Sciences

2017

This thesis entitled:
Study of the Unsteady Aerodynamics associated with a Cycloidally Rotating Blade
written by Nishant Agarwal
has been approved for the Ann and H.J. Smead Department of Aerospace Engineering Sciences

_____
Dr. John Farnsworth

_____
Dr. Lakshmi Kantha

_____
Dr. John Evans

Date _____

The final copy of this thesis has been examined by the signatories, and we find that both the content and
the form meet acceptable presentation standards of scholarly work in the above mentioned discipline.

Agarwal, Nishant (M.S., Aerospace Engineering Sciences)

Study of the Unsteady Aerodynamics associated with a Cycloidally Rotating Blade

Thesis directed by Dr. John Farnsworth

Cycloidal Rotors have been studied for over 100 years, with a focus on applications for vertical axis wind turbines (VAWTs) for energy production and vertical-take-off-and-landing (VTOL) vehicles. Although, numerous experimental and analytical studies have demonstrated their potential competency compared to conventional horizontal-axis rotors, it is not until recently that the focus of these studies has shifted towards understanding the fundamental science behind how these complex systems function. The present study extends the existing fundamental knowledge about cycloidal rotors by particularly focusing on the unsteady aerodynamic phenomena associated with a single-fixed NACA 0012 blade cycloidal rotor as the system translates across an advance ratio ($\mu = \frac{U_\infty}{\omega R}$) of 1. This phenomena was studied both experimentally, making use of particle image velocimetry (PIV) measurements on the system, and computationally, making use of both simple analytical tools and two-dimensional Unsteady Reynolds-Averaged Navier Stokes computational fluid dynamics (URANS-CFD) simulations. It is important to study the transition of the system through $\mu = 1$ in order to better understand the incapability of VAWTs to self-start, and also the progression of VTOL vehicles into forward flight. When the advance ratio is less than one the blade cuts through its own wake. As it approaches one the local airspeed of the flow over the airfoil approaches zero during the retreating portion of the cycle. Finally, as the advance ratio increases beyond one the airfoil will experience reversed flow relative to its direction of rotation. The analysis of the PIV results show that the flow just downstream of the rotor is similar for cases at the same advance ratios, and that the wake structures do not depend upon the Reynolds number, within the range investigated. The phase-history velocity contour plots of the wake structure show a distinct cycloidal pattern for the advance ratio of $\mu = 1.25$, a more stationary wake pattern for $\mu = 1$, and a retarding wake pattern for $\mu = 0.75$. CFD analysis using three different turbulence models showed that an asymmetric wake was generated behind the rotor with a more complex structure (both inside and outside the rotor diameter). This asymmetric wake generation is attributed to the difference in flow conditions at the advancing and retreating sides of the cycle. The complex structures

account for the occurrence of dynamic stall, shedding of wake from the trailing edge, flow reversal on the airfoil in the cycle, and the wake-blade interaction. Also, it is observed that a region of high velocity is generated by the airfoil as it sweeps through the flow, which interacts with the airfoil at a later point in the cycle and affects the net force on the airfoil. It was seen that the blade-vortex interaction is not a characteristic property of the cycloidal rotor system. Rather, it depends on the advance ratio at which the system operates.

Acknowledgements

I would first like to thank my thesis adviser Dr. John Farnsworth of the Ann and H.J. Smead Department of Aerospace Engineering Sciences at University of Colorado Boulder. The door to Dr.Farnsworth office was always open whenever I ran into trouble or had a question about my research or writing. He consistently supported me throughout my thesis with his immense patience and knowledge whilst allowing me the room to work in my own way.

I would also like to thank the rest of my thesis committee members for their insight and valuable discussions: Dr.Lakshmi Kantha, and Dr.John Evans. Without their passionate participation and inputs, my learning would have been incomplete.

I would also like to thank Matt Rhode, Trudy Schwartz, and rest of the AES Machine and Instruments shops team for their assistance in machining the experimental model components. I would also like to acknowledge the contributions made by Joseph Straccia and rest of my colleagues at the Experimental Aerodynamics Lab (CU Boulder) for being their whenever I needed them.

Finally, I must express my very profound gratitude to my parents for making many sacrifices and teaching me how to stay strong in the time of adversity, my sister (Sonal), brother-in-law (Shashank), and friends (Ankit, Aastha, Udit, Aakanksha, and Apurva) for providing me with unfailing support and continuous encouragement throughout my years of study. This accomplishment would not have been possible without them. Thank you.

Author

Nishant Agarwal

Contents

Chapter

Tables

Table

Figures

Figure

Chapter 1

Introduction

The cyclogyro, or cyclocopter, is an aircraft design that uses cycloidal rotors as the principle source of lift, propulsion, and control. They are capable of vertical takeoff, landing and hovering performance like a helicopter, without the same disadvantages such as limited forward speed, very high noise and vibration levels, limited flight altitude, etc. A cycloidal rotor is a horizontal axis propeller capable of producing thrust in or extracting energy from a fluid. Such a mechanical system allows for the generation of a net aerodynamic force perpendicular to the axis of rotation (Figure 1.1), which can be easily controlled in terms of magnitude and direction [35, 38] by mechanically controlling the pitching schedule and pitching amplitude of the blades [24, 2, 32]. Figures 1.2, 1.3, and 1.4 show the examples of the control mechanisms used for the purpose of blade pitching.

In the marine hydrodynamics community, this propulsion type is commonly referred to as a Voith Schneider propeller which is pictured in Figure 1.5. In the aerodynamic community, these propellers are simply refereed to as cycloidal propellers or rotors, while the novel vehicle designs that employ these for
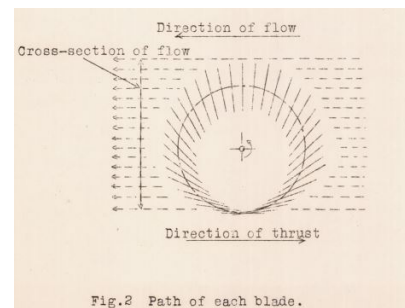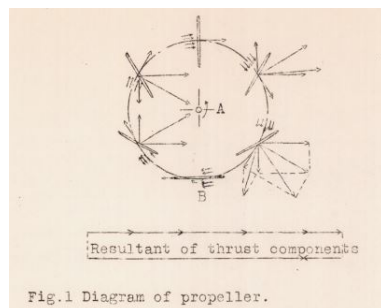
Figure 1.1: Kristen's cycloidal rotor Concept [35]
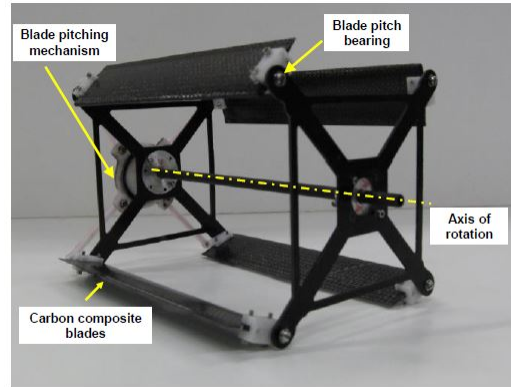
Figure 1.2: Swashplate controlled pitching mechanism from Jarugumilli [24]
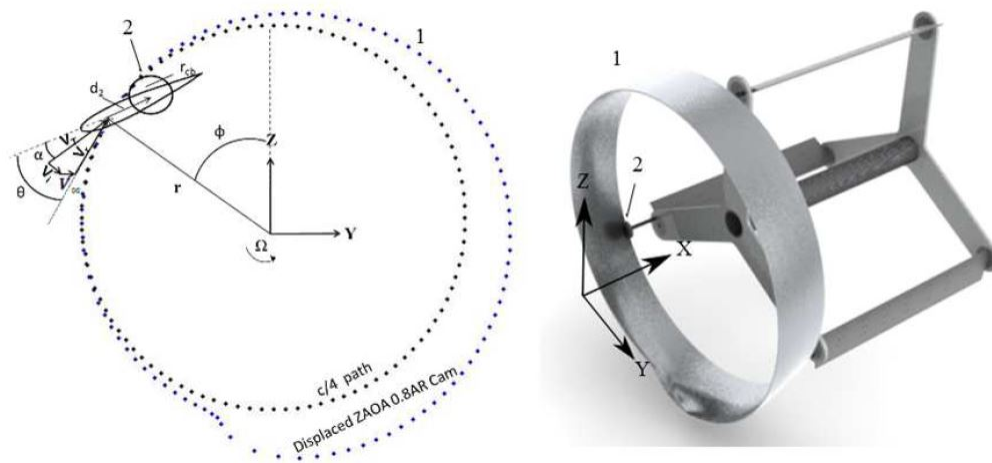
Figure 1.3: Cam-guide controlled pitching mechanism from Adams and Fagley [2]
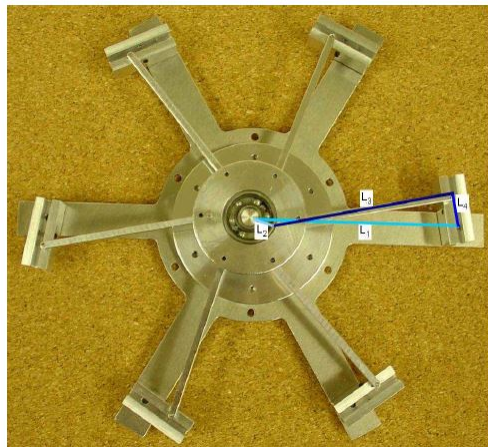
Figure 1.4: Swashplate controlled pitching mechanism from Parsons [32]

both lift and propulsion are often coined cyclogyros. The ability to vary the direction and magnitude of thrust, operate more quietly and at higher advance ratios than traditional rotors makes them attractive for a wide range of aircraft applications [27]. They can improve the maneuverability of the aircraft for several flight conditions, e.g. VTOL (Vertical Take-Off and Landing) and STOL (Short Take-Off and Landing), hovering and forward flight conditions [36]. Yu et al. [47] used an Unsteady Vortex Lattice Method to investigate the influence on the performance of the rotor to changes in the blade taper, aspect ratio, and wing-tip geometry.

Figure 1.5: Twin Voith Schneider propeller with thrust plate on a tug's hull in dry-dock. [41]

It has been demonstrated that an optimized cycloidal rotor can generate higher thrust per power input (higher power loading) when compared with a conventional screw propeller, operating at a similar disk load (thrust generated per unit area on the rotor actuator disk) [11, 8].

The aerodynamic efficiency of a cycloidal rotor depends on several design parameters, e.g. number of blades, airfoil section, blade flexibility, blade camber, blade span, rotor solidity, blade planform and blade kinematics [8, 45, 25, 48].

Compared to a conventional rotor, each spanwise blade element of a cycloidal rotor operates at similar aerodynamic conditions (i.e., at similar flow velocities, Reynolds numbers, and angles of attack), and so the blades can be more easily optimized to achieve the best aerodynamic efficiency, at least in principle. Moreover, because the blades are cyclically pitched once per revolution (1/rev), unsteady flow mechanisms may delay blade stall onset and thus augment the lift produced by the blades.

The cycloidal rotor takes its name from the cycloidal path its blades trace out relative to the air during forward flight. Figure 1.6 shows a kinematic representation of the relative blade path for various advance ratios [14]. It represents the motion traced out by the blades in forward flight, demonstrating the cycloidal shape when viewed from the side. This motion is not unlike that of winged insects and birds.
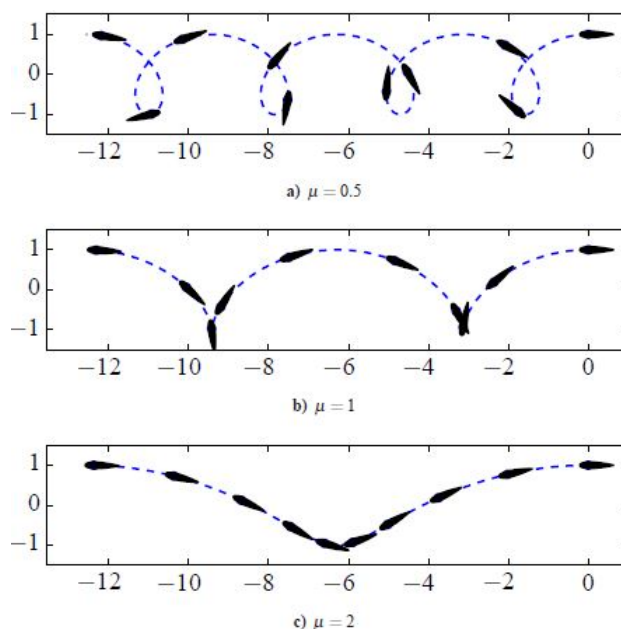
Figure 1.6: Blade paths for different advance ratios, μ, a) curtate, b) unity, and c) prolate [14].

Siegel et al. [36] explored the ability of cycloidal rotor to generate thrust by creating a flow pattern that is the inverse of the von Karman vortex street in the fluid (Figure 1.7). They made use of the unsteady fluid dynamics of the cycloidal rotor system to produce similar efficiencies as dynamic pitch and heave motions used in flapping wing mechanisms (Figure 1.8).

The cycloidal rotor lifting and propulsive forces are generated very similarly to the aileron and elevator controls on a traditional fully articulated helicopter rotor, where cyclic control inputs vary the angle of attack of the rotor blades individually as they rotate relative to the helicopter. For the cycloidal rotor, the blades are oriented in a paddle-wheel arrangement, and maintain a tangential angle relative to their path when there is no control input. When a control input is applied, the blades angles relative to their path oscillate with a magnitude, phase angle, and pitch offset dependent on the physical control mechanism. The net thrust that results is highly dependent on the design of the control mechanism and advance ratio, but in all cases
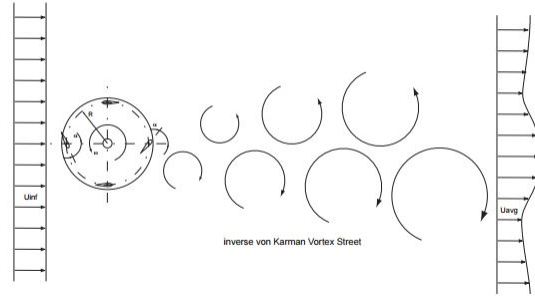
Figure 1.7: Energy injection wake explanation for thrust generation from Siegel et al. [36]
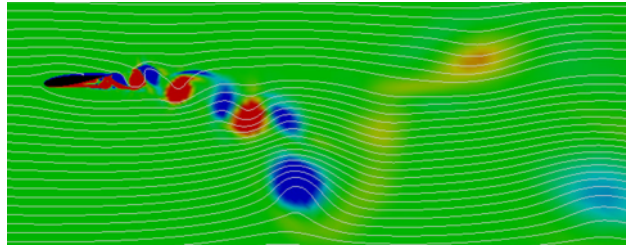
Figure 1.8: Instantaneous vorticity for an airfoil in pitch-and-heave motion from Siegel et al. [36]

it can be varied throughout the 360° cycle in the plane perpendicular to the axis of rotation. Furthermore, the cycloidal rotor has mathematically and experimentally been deemed capable of autorotation [13, 43]. This phenomenon is very important to the safety of helicopter flight, and may help to ensure the safety of a cyclogyro in flight.

1.1   History

Attempts to build flight-capable cyclogyros began in the early 20th century [10, 26, 31], where almost all attempts were applied toward full-scale manned aircraft. One of the cyclogyros built in 1930's by Schroeder is shown in Figure 1.9 [10]. However, even though there have been many such attempts, none of them were successful in building a flying cyclogyro.

One of the main reasons for this is the fact that the structural design of a cycloidal rotor is extremely challenging, owing to the significant blade strength required to handle the large centrifugal loads while minimizing the weight for use in flight. Unlike a conventional rotor, on a cycloidal rotor blade the centrifugal force acts in the transverse direction and therefore the blade design has to be stiff enough to limit transverse bending and torsional deformations. The need for high bending and torsional stiffness resulted in heavy blades due to the lack of high strength-to-weight ratio materials at that time. Furthermore, the weight of the blades further increased the rotor structural weight, because the structure and pitching mechanism had to be strong enough to handle the large inertia associated with the heavy blades. This resulted in cycloidal rotors that were considerably heavier than their conventional counterparts. These structural design issues were further exacerbated by the early attempts to make very large scale propellers for manned aircraft only. Due to these problems building a flight-capable cyclogyro proved in-feasible at the time.

In contrast, these intriguing devices have been readily used for hydrodynamic propulsion since the turn of the twentieth century as a form of tugboat drive system. This propulsion type is commonly referred to as the Voith Schneider propeller, which is pictured in Figure 1.5. Today, cycloidal rotors are readily pursued as an alternative propulsion method for micro aerial vehicles (MAVs), vertical takeoff and landing (VTOL) vehicles, and airships or dirigibles. Figure 1.10 shows an airship built by Bosch that uses cycliodal rotors for propulsion and attitude control. Different groups around the world are beginning to achieve successful

Figure 1.9: Physical example of an early cycloidal rotor aircraft [48]

Figure 1.10: AUTOBLIMP by Bosch, Oregon [11], which makes use of cycloidal rotors for steering and propulsion

untethered flights with various MAV prototypes. For instance, Benedict [1] showed autonomous hover with

Figure 1.11: Physical model of a cycloidal rotor system from Yun and Park [48]

a 200 g twin-rotor cyclogyro depicted in Figure 1.12. Adams [2] achieved controlled hover with a cyclogyro employing a novel cam based pitching mechanism, designed to allow for a seamless transition from hover to forward flight (Figure 1.3). Using this design, the cyclogyro could attain not only hover, but significant forward flight speeds as well. Another example is the cyclogyro model designed by Yun and Park [48] which is shown in Figure 1.11.

Figure 1.12: Twin cycloidal rotor in hover from Benedict et al. [5].

Several attempts have been made to better configure cycloidal rotors for wind energy applications in the form of vertical axis wind turbines (VAWTs), which have been shown to perform well in urban applications with dynamically changing wing directions. Most of this work has focused at a blade chord based Reynolds numbers on the order of $Re_c = \mathcal{O}(10^5)$ and utilized Unsteady Reynolds-Average Navier-Stokes (URANS) simulations with various turbulence models to investigate the two-dimensional flow field produced by multi-bladed VAWTs. Wang et al. [42] focused on investigating dynamic stall in a VAWT numerically by studying a 2D airfoil undergoing the effective sinusoidal pitching motion. They use the

standard k-omega and SST k-omega turbulence model to validate the experimental results, and conclude that the SST k-omega model can predict the experimental data with reasonable accuracy, other than at very high angles of attack where the flow is fully detached and the 3D effect is expected to be more significant. Figure 1.13 shows an instance of dynamic stall on the airfoil from their study.
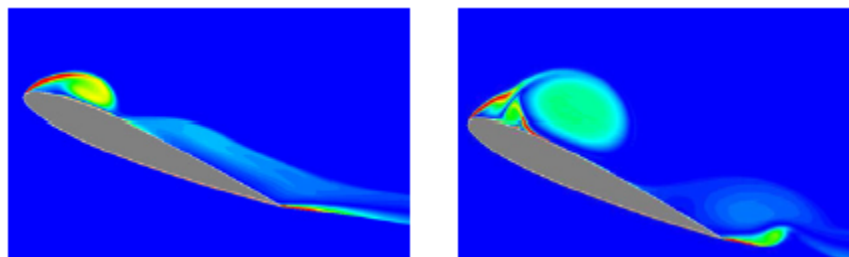
Figure 1.13: Vorticity field for the upstroke pitching phase using the SSTkω model from Wang et al. [42].

Ferreira et al. [15] simulated dynamic stall in a section of a VAWT using Detached Eddy Simulation (DES) at $Re_c = 5 \times 10^4$ and validated the results by comparing the vorticity field in the rotor area with particle image velocimetry (PIV) measurements. Figures 1.14 depicts the PIV result form their study showing the evolution of leading-edge vortex and wake shedding.

Kim et al. [22] developed a cyclogyro with four cycloidal rotors. Their test flight confirmed that the cycloidal propellers provided enough thrust for stable and controlled flight. The tethered test in hover flight is shown in Figure 1.15.

Benedict [8] concluded that the cycloidal rotor has higher hovering efficiency than a traditional screw rotor. Their analysis also showed that aero-elastically induced twist of the blade structure can result in smaller aerodynamic force production. Furthermore, they also developed a remote controlled cyclogyro that flew with good stability.

Jarugumilli [24] examined the time-averaged aerodynamic force and power measurements through parametric studies using PIV and CFD techniques. Figure ?? shows the flow through the rotor from the PIV study, and Figure ?? shows the pressure distribution on the rotor from CFD analysis.

Yang [46] integrated an aero-elastic blade model into the Overflow CFD code and performed numerical simulations with several cycloidal propellers. Their analysis indicated that both two dimensional and three
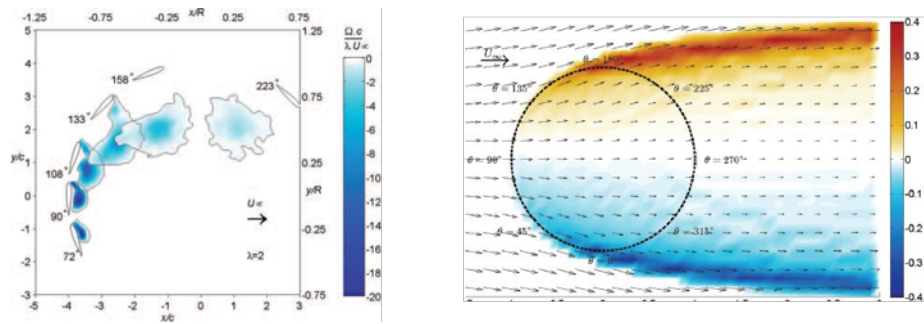
Figure 1.14: PIV experimental data of the (a) evolution of the circulation of leading-edge separated vortex for $\lambda = 2$ [15], (b) time-averaged vorticity distribution for $\lambda = 4$ [20] from Ferreira et al.
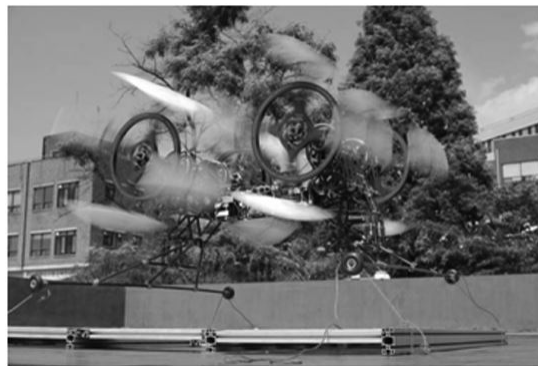
Figure 1.15: 4 cycloidal rotor powered cyclogyro in Hover flight [22]
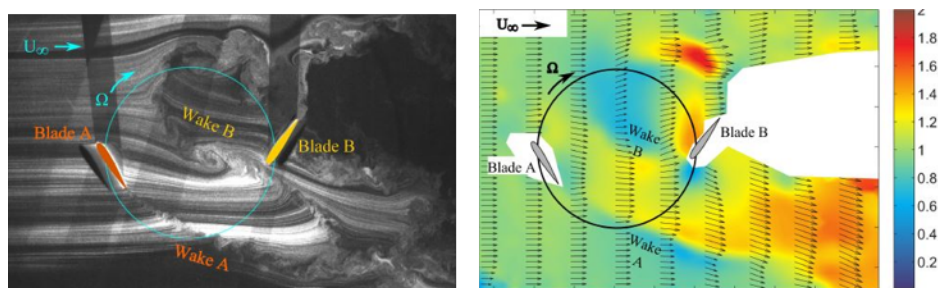
Figure 1.16: Flow field using PIV flow measurement technique from Jarugumilli [24]
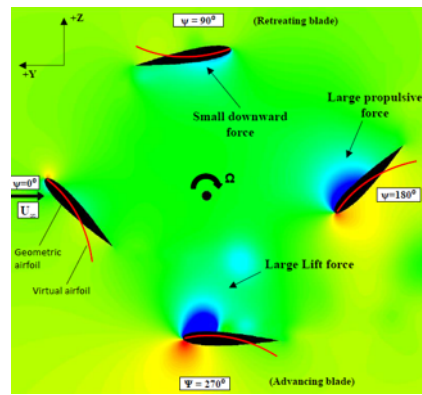
Figure 1.17: Pressure distribution on the rotor using CFD technique from Jarugumilli [24]

dimensional simulations can produce results which were quite similar to the experiment results. Xisto et al. [44, 45] performed analysis on the effects of the various geometric parameters of a large scale cycloidal rotor. Figure 1.18 shows the velocity contours from the CFD analysis of four different blade configurations, depicting the change in exit flow direction and magnitude with the number of blades. They concluded that the best chord to radius ratio was $c/R = 0.5$ and the best location of the blade pitching axis was $x/c = 0.35$ from the leading edge.

In Europe a major multi-country project consortium was set up to advance research on human carrying vehicles propelled by cycloidal rotors. This is the goal of the CROP (Cycloidal Rotor Optimized for Propulsion) project [40]. The objectives of this consortium was to analyze the influence of four key design parameters on the rotor's aerodynamic efficiency. An analytical tool was therefore developed for predicting the overall thrust generated and power required by the cycloidal rotor. Such a model is also able to generate, for a set of geometrical inputs, an instantaneous design and animation of the selected configuration. This allowed for a detailed kinematic analysis of the rotor blades and the mechanical system. The proposed analytical model was validated with experimental data for a six-bladed rotor configuration, which was carried out by the Austrian company IAT21, a partner of the CROP project (Figure 1.19). A CFD study was also conducted to provide a deeper insight in the complex flow patterns that characterize the aerodynamics of a cycloidal rotor. Both techniques were employed to study: 1) the influence of the airfoil section geometry (in particular its thickness), 2) the number of blades (which is critical in defining the so-called rotor solidity
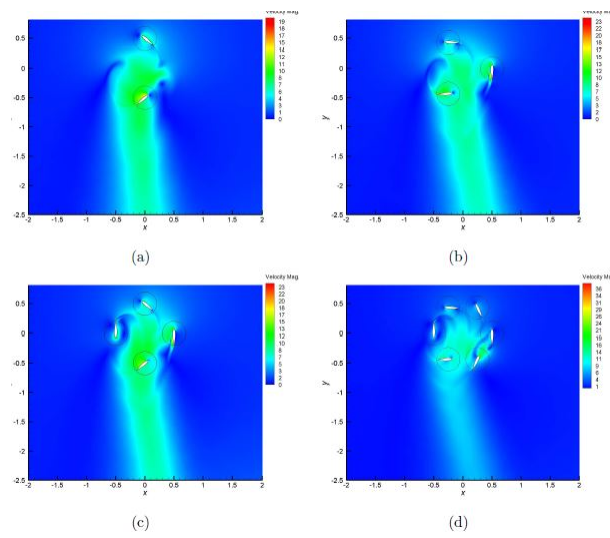
Figure 1.18: CFD analysis of different cycloidal rotor blade configurations from Xisto et al. [45]

Figure 1.19: An artistic rendering of the IAT21 D-Dalus craft which is develped under the CROP project. [40]

parameter), 3) the chord-to-radius ratio, and 4) the pitching axis location. It is expected that these four parameters have a strong influence on the overall performance of a large-scale cycloidal rotor, as those envisaged by the CROP project for potential application to a future generation of manned aerial vehicles [40]. Computational tools have been widely used for analyzing the influence of several fluid-dynamic effects on the aerodynamic behavior of pitching airfoils [18], rotary wings and on the efficiency of cyclogyros [38]. It has been demonstrated, through the usage of various numerical tools, that the unsteady interference among blades can significantly alter the flow uniformity on the downstream blades, affecting their aerodynamic performance [23]. Such an interaction may improve the rotor's thrust generation by delaying stall on each individual blade [33], but it could also reduce their efficiency. The flow on the cycloidal rotor was also experimentally analyzed using particle image velocimetry (PIV) measurements. From these studies complex flow patterns have been observed, such as: 1) the formation and advection of the leading edge vortex on the pitching airfoils [8], 2) the generation of large regions of rotating flow inside the rotor cage, and 3) a skewed exit flow [7]. For analyzing the flow on cycloidal rotors several analytical models have been developed so far. Wheatley [43] formulated a simplified aerodynamic model for the cycloidal rotor by neglecting the unsteady aerodynamic effects. Sixty eight years later McNabb [29] took into account the unsteady aerodynamics by using the model of Garrick [17] in his formulation, and validated his work by comparing the results obtained with the experimental data of Wheatley [43] and Bosch Aerospace [29]. Yun et al. [44] proposed an analytical model based on blade element theory and on the streamtube model. In their model a control volume is defined, to which the conservation of mass, momentum, and energy are applied. Sirohi et al. [37] introduced an analytical model which was able to predict rotor performance, where vertical axis wind turbine theory was adapted into the context of aeronautical propulsion.

1.2   Motivation

The key advantages of utilizing a cycloidal rotor system are its higher aerodynamic efficiency and potential for low noise and increased maneuverability. Unlike a conventional screw rotor, where aerodynamic conditions vary significantly along the blade span, all span-wise blade elements of a cycloidal rotor operate under similar aerodynamic conditions (i.e. low velocities, Reynolds numbers, and angles of incidence). This allows every section of a cycloidal rotor blade to operate at the peak aerodynamic efficiency. Previous studies have shown that a cycloidal rotor can achieve higher values of power loading (thrust/power) compared to a conventional rotor of the same scale [5].

Furthermore, the relatively uniform span-wise distributions of aerodynamic forces can allow the cycloidal rotor to operate at a lower tip speed compared to a conventional rotor for a given thrust value, potentially leading to a reduction in the noise signature of a rotorcraft vehicle. A third advantage of the cycloidal rotor is its unique thrust vectoring capability. The resultant force vector of the rotor can be instantaneously set to any direction perpendicular to the axis of rotation, providing full 360° control authority. Thus, a cycloidal rotor-based aircraft may observe better maneuverability compared to a conventional rotor-based MAV, making it ideal for operations in highly confined and gusty environments.

The flow around a cycloidal rotor system is dominated by unsteady aerodynamics which is due to the vast time-dependent, changes in the sectional angle of attack, and the dynamic inflow that is the influence of the shed wake vorticity on the inflow velocity of the rotor blade. The level of unsteadiness is typically quantified by the reduced frequency of the flow over the airfoil k, defined as $k = \omega c/2U$, where ω is the angular frequency of rotation, c is the blades chord and U is the free-stream velocity. In case of VAWT, the condition of unsteady aerodynamics is necessary for its operation, since its energy exchange depends on the time variation of bound circulation over the rotation, following Kelvins theorem. Even considering low reduced frequency conditions, the flow over the airfoil can be treated as quasi-steady, but the overall flow of the rotor, in particular the wake, will be unsteady [12].

As a result, the challenge for designing this system is to understand its flow dynamics to quantify the effects of various parameters on the net forces produced. The increased complexity in the flow dynamics

is due to superposition of various phenomena such as: 1) virtual camber, Coriolis forces [39], 3) complex wake-blade interactions, 4) effects of tip speed ratio or advance ratio, 5) highly unsteady pitch and heave motions, 6) radial velocity (pressure) gradients, 7) centrifugal forces on the Boundary layers, 8) blade bending, etc. Hence, the aim of this study is to understand the influence of a few basic flow characteristics as a function of Advance ratio, μ, without concentrating on the optimization of the performance of a particular configuration. An attempt has been made to study both the global and local effects of this parameter using both computational simulations and experimental measurements of the fundamental system.

1.3   Working Principle

To understand these complex aerodynamic features, it is important to first understand the fundamental kinematics of a cycloidal rotor. The blade path throughout a cyclic revolution is a direct function of the ratio between the free-stream velocity, U_∞, (i.e. forward flight) and angular velocity due to rotation, ωR. This is commonly referred to as the advance ratio, which is mathematically defined as,

$$\mu = \frac{U_\infty}{\omega R}.$$

For a cycloidal rotor, the advance ratio defines three distinct kinematic profiles, namely, curtate ($\mu < 1$), unity ($\mu = 1$), prolate ($\mu > 1$). The unraveled blade path at a neutral angle of attack is pictured for each of these cases in Figure 1.6. Note the neutral angle of attack is defined when the blade is directly oriented into the relative, incoming flow (i.e. zero angle of attack), then the device becomes feathered and minimal thrust and drag are achieved for a given blade geometry [14].

In forward fight, the top half of the cycloidal rotor ($270° < \theta < 90°$) is the "advancing" side, and the bottom half of the rotor ($90° < \theta < 270°$) is the "retreating" side. For the purpose of understanding the dynamics of the system, the rotating cycle can be divided into four quadrants, as shown in Figure 1.20. The radial distance from the rotor axis of rotation to any point on the blade surface (or chord) is unique. Taking this radius into proper consideration when defining the rotor geometry leads to a mathematical expression for the local angle of attack, α, and relative inflow velocity, V_R. This is due to the phenomenon of "virtual camber" discussed below. For the setup used in this research the blade mounting point was at the quarter
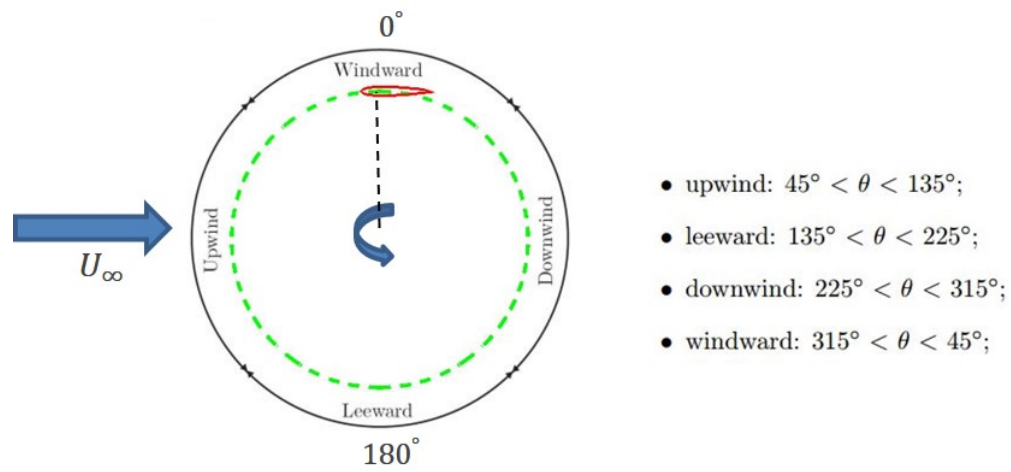
Figure 1.20: Schematic of the blade kinematic motion and operating regions

0°
Windward
Upwind
Downwind
Leeward
180°
U_∞

- upwind: $45° < \theta < 135°$;
- leeward: $135° < \theta < 225°$;
- downwind: $225° < \theta < 315°$;
- windward: $315° < \theta < 45°$;

chord, $x/c = 0.25$. Mechanisms such as rotational circulation, wake capture, and the unsteady leading edge vortex do seem to properly account for the aerodynamics forces. The unsteady leading edge vortex involves leading edge flow separation that reattaches to the wing and forms a separation bubble. The vortex increases the circulation around the wing and creates much higher lift than in the steady-state case. This vortex remains stable due to its highly three-dimensional nature [21]. Also, the added rotational velocities will alter the pressure distribution and boundary layer of the airfoil, leading to a change in force distribution and system efficiency.

VIRTUAL CAMBER: is an aerodynamic phenomenon commonly found on vertical axis wind turbine blades where due to the orbital motion of the blades they experience curvilinear flow. Blades subjected to a curvilinear flow behave very differently compared to being immersed in a rectilinear flow. In a curvilinear flow, the local velocity and angle of attack of the blade are unique at different locations along the blade chord. As a result, a symmetric blade at $0°$ pitch angle in a curvilinear flow can be viewed to behave like a cambered blade at an angle of incidence (α_i) in a rectilinear flow. This effect will be more pronounced in cycloidal rotors having large chord-to-radius ratios, c/R [4]. In the absence of free stream velocity, the local angle of attack of the resultant velocity along the chord can be simply defined for any arbitrary location on the chord, x, by

$$\alpha_x = arctan(x/R).$$

Now this scenario is approximately equivalent to having a cambered airfoil, with the camber line slope (dy/dx) equal to α_x in a rectilinear flow of magnitude ωR. Figure 1.21 presents a basic, visual definition virtual chamber.

However, in the presence of a free stream velocity the virtual camber of the airfoil changes throughout the cycle. The schematic for this condition is shown in Figure 1.22. The magnitude of the relative local inflow velocity at any point along the chord is given by

$$V_R' = [(\omega R')^2 + (V_\infty)^2 - 2V_\infty \omega R' sin\,\theta']^{1/2}$$

where

$$\theta' = \theta - \Delta\theta,$$

(a) Virtual Camber in Rectilinear Flow

(b) Schematic explaining Virtual Camber
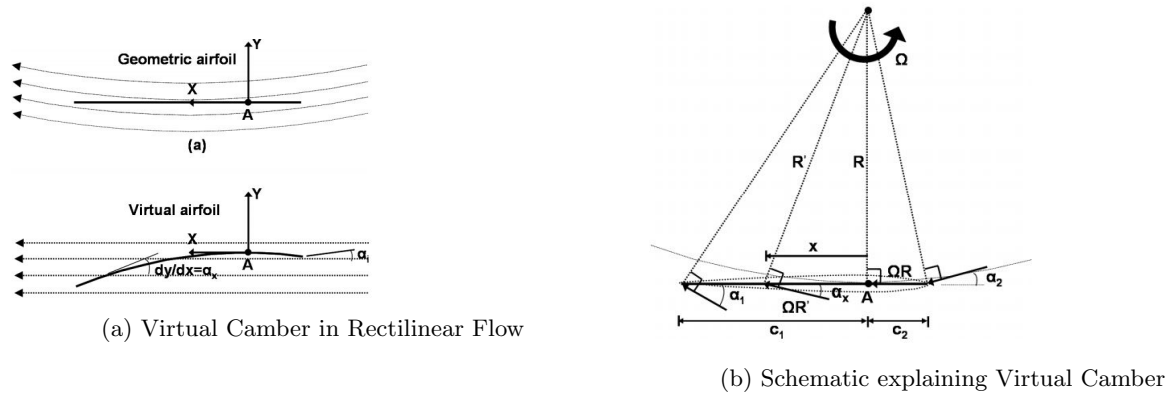
Figure 1.21: Virtual Camber effect in the absence of Free Stream [4]

$$\Delta\theta = -arctan\left(\frac{x}{c}\frac{c}{R}\right),$$

$$R' = R/cos\Delta\theta$$

and

$$R'^2 = R^2 + x^2.$$

As a result the local advance ratio can be defined as

$$\mu' = \frac{V_\infty}{\omega R'} = \mu cos\left(\Delta\theta\right),$$

which allows the magnitude of the relative local inflow velocity equation to be written as

$$V_R' = \omega R'\left(1 + \mu'^2 - 2\mu' sin\theta'\right)^{1/2}.$$

The angle ϕ, which is the angle between the rotational velocity (ωR) and the relative local inflow velocity (V_R'), may be found now from the relation

$$\frac{V_\infty}{\sin\phi} = \frac{V_R'}{\cos\theta'}$$

$$\phi = arctan\frac{\mu' cos\theta'}{(1 - \mu' sin\theta)'}$$

The local angle of attack is then defined as

$$\alpha' = \phi - \Delta\theta.$$
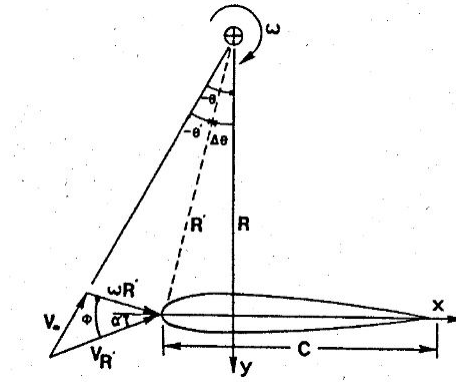
Figure 1.22: Virtual Camber effect in the presence of Free Stream [30]

The variation of the flow curvature at different azimuth locations for a flat-plate fixed tangentially to the rotational circle at the quarter chord ($x/c = 0.25$) of the flat plate is discussed in the next section. Because of the large chord to radius ratio ($c/R = 0.5$) of the current rotor, there is significant virtual camber throughout the cycle which is expected to play a significant role in the aerodynamic performance of the rotor. Note that these transformation equations for virtual camber were origonally provided by Wolfe et al. [30].

BOUNDARY LAYER CENTRIFUGAL EFFECTS: where observed and discussed in studies conducted at both Delft University of Technology and West Virginia University [30]. The boundary layer that develops over the airfoil is dragged along with it as the airfoil rotates. However, the fluid particles also feel an outward centrifugal force acting on them due to the rotation, which leads to the modification of the boundary layer profile near the surface. The equations for the pressure gradient through the boundary layer, derived by Wolfe et al. [30] using the incompressible Navier-Stokes equation, show that the order of the pressure gradient (perpendicular to the surface) for a tip speed ratio of 3 or more, is at least an order of magnitude larger than that resulting from curved flows. They showed that the pressure gradient is proportional to the square of the tip speed ratio. This may lead to adverse boundary layer separation with a loss of lift and increase in drag. However, as the angle of attack cyclically changes sign over the cycle, the orientation of the low pressure surface of the blade also varies cyclically. The separation might be delayed on the upstream side of the rotor and accelerated on the downstream side, however not much work has been done to evaluate how this effects the performance of a cycloidal rotor system.

DYNAMIC STALL: refers to the delay in the stall of airfoils that are rapidly pitched beyond their static stall angle of attack. It is associated with a substantially higher lift than is obtained quasi-statically. Due to the large variation in the local angle of attack, dynamic stall occurs on VAWTs operating at low tip speed ratios. Furthermore, the pinch-off of the dynamic stall vortex (leading-edge vortex, LEV) causes a sudden decrease in the lift, a rapid increase in the drag, and a nose-down pitching moment [39].

BLADE WAKE INTERACTION: occurs as a cycloidal rotor blade crosses the wake it has previously generated (or wakes generated by other blades) during the windward, downwind and leeward sections of the rotation cycle. The number of interactions between blade and wake is a function of number of blades, tip-speed ratio (advance ratio) and loading of the rotor. Blade-wake interaction is particularly important due to the resulting pressure distribution fluctuations over the airfoil, which create variations in the lift and drag, but also typically result in increased noise [16].

Chapter 2

Geometric Design

The cycloidal rotor system is designed to test a rotating airfoil with it's chord parallel to the axis of rotation, at a radial distance of 165.1 mm (6.5 in) from the axis. Tests were conducted with a single NACA 0012 airfoil having a chord length of 82.55 mm (3.25 in), which is equivalent to 1/2 of the radial length ($R/2$). Also note, that the airfoil was geometrically fixed to have a zero-degree geometrical angle of attack relative to the rotation path (i.e. the airfoil chord was perpendicular to the radius of rotation. That said the instantaneous angle of attack, α, is varies along the airfoil chord while the airfoil is rotating due to the virtual camber effect. Moreover, the local angle of attack is a function of the rotational speed and the free-stream velocity (or advance ratio μ).

2.1 Virtual Camber and Flow Curvature

As discussed earlier, virtual camber plays an important role in determining the aerodynamic characteristics of a rotating airfoil. The airfoil undergoes a large variation in angle of attack as it rotates around the axis. Figure 2.1 shows this variation of angle of attack at the quarter chord ($x/c = 0.25$) as a function of azimuthal angle, θ. It can be seen that at the $\theta = 180°$ position in the cycle the airfoil executes an instantaneous flip in its direction relative to the flow for an advance ratio greater than 1. At advance ratio of exactly equal to one the local angle of attack on the airfoil changes direction by $180°$ at the same azimuthal position in the cycle. Below μ of 1, the change in direction is more gradual. Figure 2.2 shows the variation in resultant velocity magnitude at the quarter chord position of the airfoil as it revolves in the cycle. The velocity magnitude gradually drops down in the first half of the cycle and rises up again in the second half.
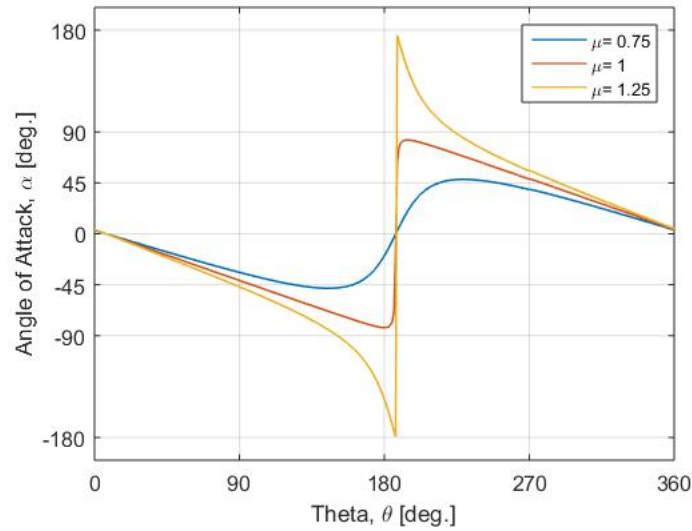
Figure 2.1: Local angle of attack, α, at $x/c = 0.25$ versus the azimuth angle, θ for three advance ratios, $\mu = 0.75, 1$ and 1.25.
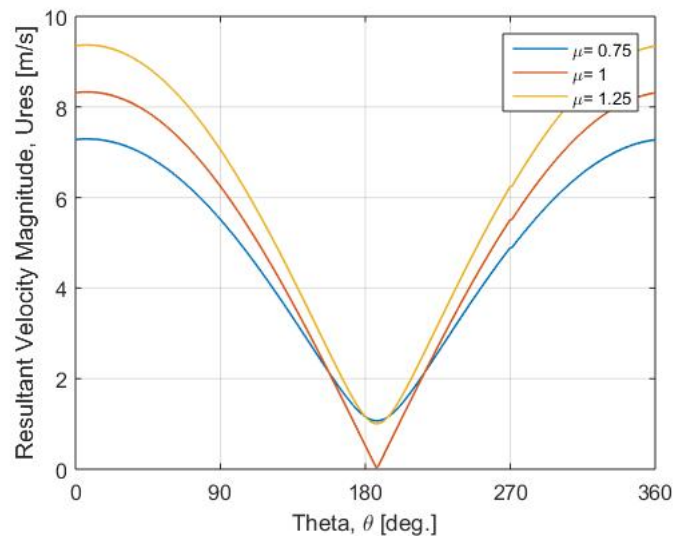
Figure 2.2: Resultant velocity magnitude versus the azimuth angle, θ for three advance ratios, $\mu = 0.75, 1$ and 1.25.
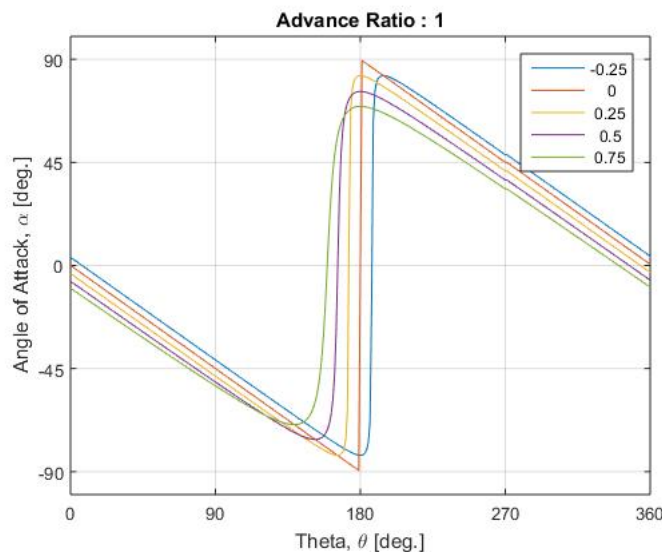
Figure 2.3: Local angle of attack, α, for $\mu = 1$ versus the azimuth angle, θ for various chordwise positions along the blade, $x/c = -0.25, 0, 0.25, 0.5$ and 0.75.

The virtual camber effect can be seen in Figures 2.5 and 2.6 which present the variation of angle of attack and resultant velocity magnitude at different chord locations in the cycle. This causes the airfoil to appear as cambered relative to the flow resulting in the generation of complex vortex structures and phenomenons like the dynamic stall.

It is observed that for a system rotating at $\omega = 240$ rpm, a blade at an azimuthal position of $\theta = 0°$ in the rotor cycle can have a variation in angle of attack of $\Delta\alpha \approx 14°$ over the chord. However, the virtual camber effect is reduced as the advance ratio increases. Due to a superposition of the virtual cambering and flow curvature effects, the rate of change of angle of attack and the resultant velocity at every point along the blade chord is different. This can be see in Figures 2.3 and 2.4.

2.2   Manufacturing of the Experimental Cycloidal-Rotor System

The experimental cycloidal rotor system was designed in a modular fashion allowing for the testing of multiple blades in multiple positions. Most of the system was machined from 6061-T6511 aluminum, which is frequently used in aircraft construction and has a tensile strength of 45000 psi. Note, that Alloy 6061-T6511 has a high strength-to-weight ratio, making it ideal for large parts that need to be very light.
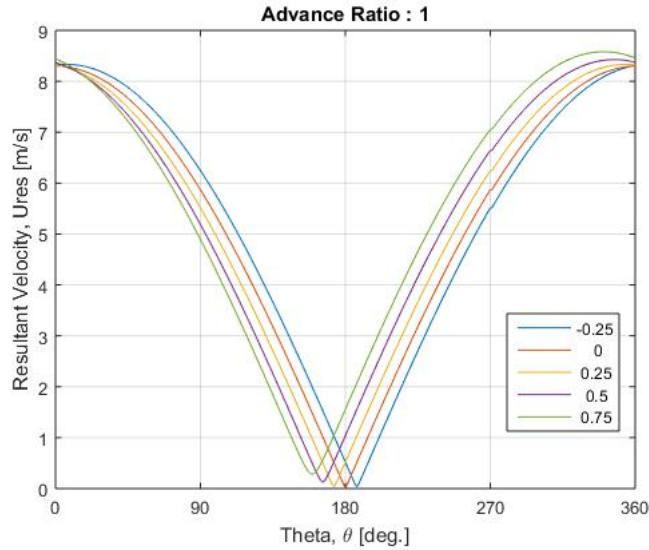
Figure 2.4: Change in Resultant velocity magnitude for $\mu = 1$ versus the azimuth angle, θ for various chordwise positions along the blade, $x/c = -0.25, 0, 0.25, 0.5$ and 0.75.
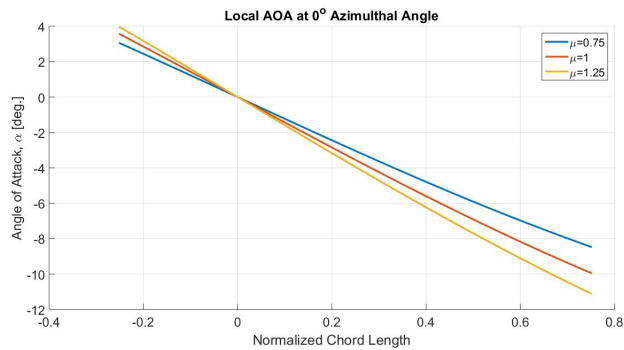
Figure 2.5: Local angle of attack, α, at $\theta = 0°$ versus the chordwise position, x/c for various advance ratios $\mu = 0.75, 1$ and 1.25.
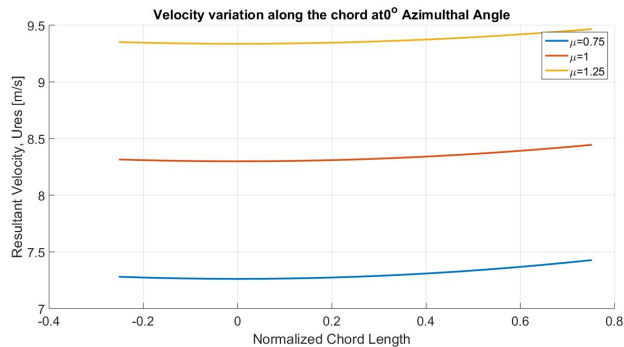
Figure 2.6: Local velocity magnitude at $\theta = 0°$ versus the chordwise position, x/c for various advance ratios $\mu = 0.75, 1$ and 1.25.
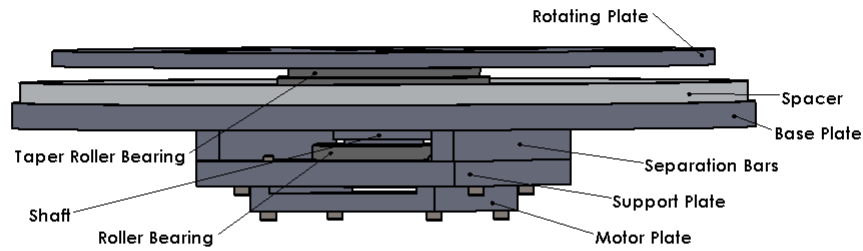
Figure 2.7: Drawing showing the manufactured system assembly (without the blade)

The system was designed as a rotating test bed with the ability to support multiple airfoil configurations. The rotating disk (floor plate) of the rotor has 416.56 mm (16.40 in) diameter and is 9.525 mm (3/8 in) thick. A drawing showing the assembly of the manufactured system is depicted in Figure 2.7.

It can support airfoils two radii , namely $R = 165.1$ mm (6.5 in) and $R = 101.6$ mm (4 in), and in three configurations: one airfoil, two airfoils (180° apart), or three airfoils (120° apart). The rotating plate (test-bed) is shown as a drawing in Figure 2.8. Note, there is no central shaft or axis protruding out of center of the rotating test bed. This eliminates any other physical disturbances in the flow, other than the blades themselves.

The rotating plate is seated on a 72.2 mm (3 in) long shaft which transmits torque from the motor to the rotating test bed. The shaft has four steps of reducing diameter and is the most critical part of the system. A drawing of the shaft is shown in Figure 2.9. The first step is a 101.6 mm (4 in) diameter flange, 5.08 mm (0.2 in) thick, on which the rotating plate sits. The stepped flange flushes with the bottom surface of the rotating plate after installation. There is a clearance fit with a tolerance of 0.005 in between the two mating parts. The rotating plate is fastened to the shaft with three $1/4 - 20$ flat socket-head screws which are countersunk in the rotating plate. The torque transmission takes place using three 0.5 in dowel pins,
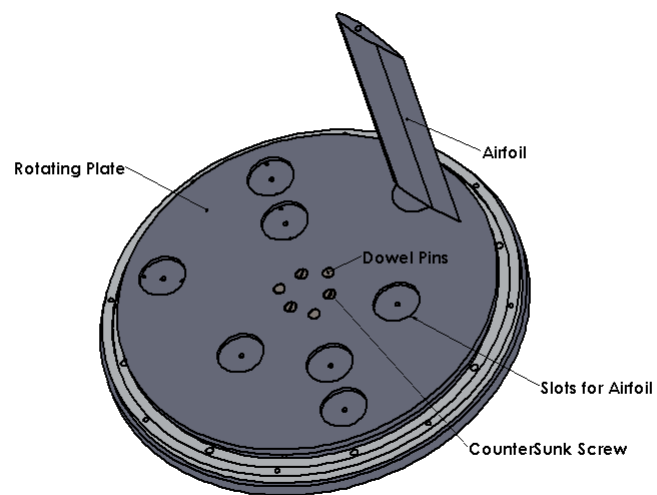
Figure 2.8: Drawing showing the test bed where blades can be installed at various configurations

which are each 1 in in length. These dowel pins are press fitted in the shaft and have a clearance fit on the rotating plate. The second step on the shaft is 82.55 mm (3.25 in) in diameter and mates with a tapered, roller bearing which is responsible for carrying most of the radial and axial system loads. The shaft has a sliding fit with the bearing's inner race. The bearing is 36.57 mm (1.44 in) thick which provides enough contact surface area between the bearing and the shaft for a close friction fit. The third step on the shaft, is 50.8 mm (2 in) in diameter and was made to sit on the face of a second, roller bearing that gives the system radial stability. The final step in the shaft is 44.45 mm (1.75 in) in diameter and mates with the inner race of the second, roller bearing.

The cup of the taper roller bearing is press fitted on a stationary circular plate which is 15.875 mm (5/8 in) thick and 457.2 mm (18 in) in diameter. This plate forms the base of the system and supports all of the other parts. The outer race of the second roller bearing is press fitted into a 177.8 mm^2 (7x7 in^2) support plate which is 15.875 mm (5/8 in) thick. This plate is attached to the base plate via $1/4-20$ socket head screws and four 1/4 in dowel pins, used to ensure proper alignment. The separating distance of these two plates is necessary for the appropriate alignment of the roller bearing, which is 19.71 mm (0.776 in) thick and is press fitted for 50% of its thickness. This is ensured by using two $20.32x15.875x177.8$ mm^3 ($0.8x5/8x7$ in^3) separation bars. The final part is a 127 mm^2 (5x5 in^2) plate that is 15.875 mm (5/8 in) thick, which is used to support the motor and is attached directly to the support plate. This plate has a 101.6 mm (4 in) slot at the center, 5.08 mm (0.2 in) deep made to allow for the screw heads to fit. The motor is bolted directly into this plate using $12-32$ phillips-head, pan screws and nuts. A ring 12.7 mm (0.5 in) in thickness and 457.2 mm (18 in) in diameter is used as a spacer between the base plate and the wind tunnel floor. The whole system is secured to the tunnel bed using eight 1.5 in long 3/8 bolts and split washers. The spacer ring is used to ensure that the rotating test bed is flush with the wind tunnel floor after installation, giving a smooth transition to the flow as it passes over the rotating system. The radial clearance between the edges of the rotating test bed and the tunnel cavity is less than 0.25 in.

The motor used in the system is a Teknic ClearPath Motion Motor. It has a torque limit of 15 Nm and a maximum rotational speed of 800 rpm. The motor was capable of velocity control, position feedback, and torque control. The positioning resolution is set by the motor encoder and is equal to 800 counts per
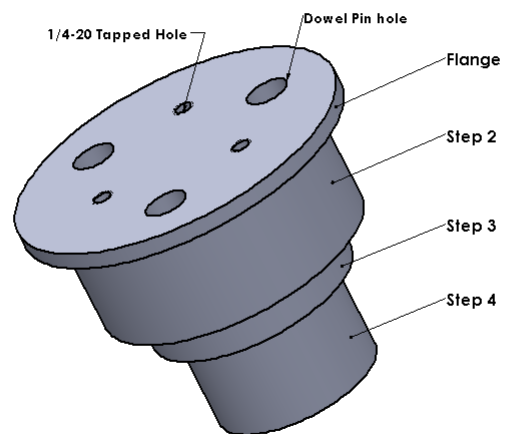
Figure 2.9: Drawing showing the shaft that helps in torque transmission between the motor and the rotating system

revolution which equates to $\pm 0.45°$.

A position control system was designed to home the motor at the desired system location. It is also used to track the system location and generate the trigger signal for the particle image velocimetry (PIV) system at the desired angular positions. This position control system was designed by using a combination of a reed switch and magnet. The reed switch is an electrical switch operated by an applied magnetic field. It consists of a pair of contacts, on ferrous metal reeds in a hermetically sealed glass envelope, which become magnetized and move together or separate when a magnetic field is moved towards the switch. The reed switch is placed in a slot in the base plate using a 3-D printed plug that supports the reed switch and is inserted into the slot. Four 1/8 in cube rare earth NdFeB magnets are press fitted together in a row on the bottom face of the rotating plate at an angular position of $90°$ phase lagged from the airfoil blade (for the one-airfoil configuration). These magnets are capable of activating the reed switch from a distance of about 1 in away. This marks the $\theta = 0°$ position of the airfoil (rotor system) which corresponds to the airfoil facing directly in the free-stream flow as shown in Figure 1.20.

The tested airfoils were 3-D printed with a standard black resin on Form 2 stereo-lithography printer. The airfoils had a NACA 0012 profile and a chord length of $c = 82.55$ mm (3.25 in). Each airfoil is manufactured in three separate sectional pieces which were assembled to form a complete 10 in span airfoil. The top section was designed with the male mating lug that is in two parts, and a smooth top surface. The middle section has a female mating slot on one end and lugs on the other. The clearance between the male-female parts was 0.005 in on each side. The bottom section has a slot on one end and a 50.8 mm (2 in) diameter circular base on the other. This base insets into the slots on the rotating plate and provides structural support for the airfoil against aerodynamic and centrifugal loads. The whole airfoil assembly is held together in compression using a 0.25 in steel threaded rod that passes at quarter chord position of the airfoil. This rod is then threaded in the rotating plate and secured by nuts and a washer. Also two 0.125 in diameter dowel pins were used to locate the airfoil base in the rotating plate slot.

The rotating system was capable of producing a large torque in a very constrained environment with sensitive instrumentation around it. As a result, great care was taken on tolerances and designing the model accurately to ensure the safety of the facility and instrumentation. The model was tested for stability on
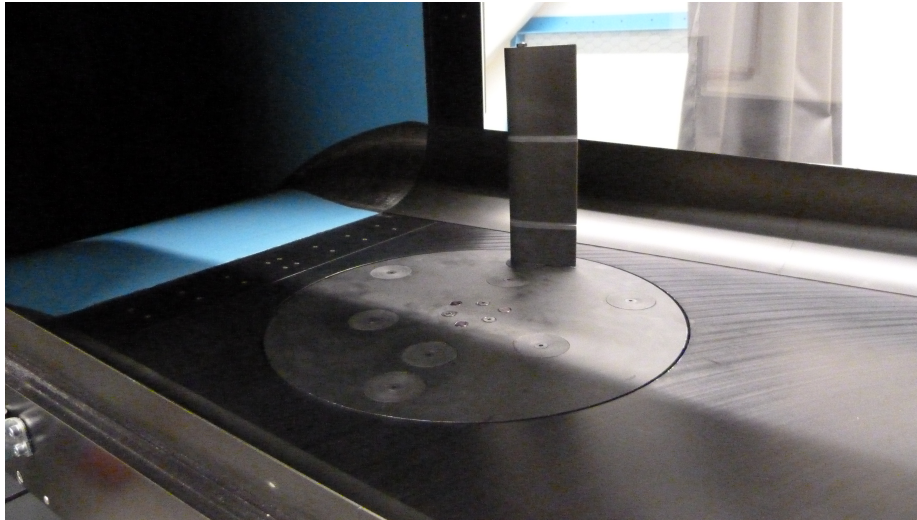
Figure 2.10: Cycloidal rotor setup installed in the CU low-speed, research wind tunnel.

a wooden bench before installation in the wind tunnel. Figure 2.10 shows the model installed in the wind tunnel.

The torque requirements of the system were approximated by using basic numerical analysis and the equation below:

$$I_{disk} = \frac{1}{2}MR^2$$

$$I_m = MR^2$$

where I is the moment of inertia for the entire rotating system. The contributions to the rotational moment of inertia from the rotating disk was 0.076 kg/m^2, from the main shaft was 0.0007 kg/m^2, and from the airfoil-rod assembly was 0.0018 kg/m^2. Note that the moment of inertia of the airfoil was found by using the equation:

$$I = 0.0384ct^3 \ [9],$$

where c is the chord length and t is the maximum thickness of the airfoil. For the two bearings the moments of inertial were estimated at 0.0013 kg/m^2 and 0.01 kg/m^2, respectively. Assuming the angular acceleration to be $\pi \ rad/s^2$, the torque required to drive the system was estimated to be 0.282 Nm. Note, that this approximation is done without considering the static and kinetic friction from the bearings. While calibrating the motor, which is rated to a peak torque of 15!Nm it was observed that the system overcomes friction and

performs free rotation at nearly 2% torque value which corresponds to 0.3 Nm. However, at higher rotation rates the centrifugal and aerodynamic forces produce an imbalance in the system requiring higher driving torques. An auto calibration was run for system rotating at 300 rpm, and was hence set at 15% peak torque for the entire testing.

The airfoil blade loading and maximum bending were numerically approximated using the Euler-Bernoulli Beam Theory. Considering the airfoil as a cantilever beam the equations are as follows:

$$\delta = \frac{(px^2)(6L^2 - 4xL + x^2)}{24EI}$$

is the equation for maximum deflection at the free end,

$$\delta_b = \frac{pL^4}{8EI}$$

gives the deflection at the point of action of the force. Here, p is in line force per unit length. Considering low-speed, a thin airfoil assumption was applied to estimate the the aerodynamic force, which was assumed to act through the quarter chord position. Also, since the steel rod passes through the quarter chord position where airfoil is the thickest it was safely assumed that the centrifugal force for the airfoil-rod rotating system is acting on the same axis as the aerodynamic force. Further assuming that the cumulative force acted in a uniform distribution along the blade span, the total force acting on the airfoil is given by

$$f_{rad} = f_{cf} + f_{aero} = m\omega^2 r + \frac{1}{2}\rho(\omega r)^2 c C_l$$

, where f_{cf} is the centrifugal force and f_{aero} is the aerodynamic force. The coefficients for aerodynamic forces are approximated using potential flow theory and blasius equation [14].

The maximum coefficient of resultant force was estimated to be 0.46. The aerodynamic force acting on the airfoil for this coefficient of lift is almost 1/45 times the centrifugal force. Using this resulting force, a negligible deflection of the airfoil tip at the local testing velocity of 10 m/s was predicted. Note that this corresponds to the case for a system rotating at 300 rpm with an advance ratio of $\mu = 1$. Also, this was verified physically by checking for any loose bolts or audible vibrations after keeping the system running for considerable amount of time. This ensured the safety of operation of the rotating system, and also that no visible significant flutter occurs to effect the aerodynamics.

Chapter 3

Computational Fluid Dynamics Simulation

Computational fluid dynamics (CFD) simulations offer an attractive and powerful method to analyze the complex and unsteady aerodynamic flow associated with a functioning of the cycloidal rotor. In this work various turbulence models were used in Unsteady Reynolds Averaged Navier-Stokes (URANS) simulations to analyze the unsteady flow through the rotor. The computational simulation and analysis was carried out through the use of an off-the-shelf comercial code, namely ANSYS's Fluent software, which can solve either the Reynolds averaged NavierStokes (RANS) or Large Eddy simulation (LES) equations. To account for the turbulence effects, which can be of random chaotic nature, the instantaneous NavierStokes equations are time-weighted averaged resulting in the well-known RANS equations. The time-weighted average procedure is based on a statistical approach applied to the main variables of the flow and decomposes velocity in to an average, $\bar{u}$, and a fluctuation term, u',the so-called Reynolds decomposition [20]. LES represents a powerful technique to represent the turbulence characteristics of a flow by decomposing it into large and small scales. The small eddies are filtered out, so that the effect of large structures can be solved using the NavierStokes equations directly, while small scale turbulent mixing is modeled. The effect of eddies smaller than a certain grid size, Δx, is estimated using a subgrid-scale model [19]. Two-dimensional simulations were carried out, and the setup was carefully controlled to ensure the simulation at equivalent conditions as expected for the experimental study. These studies were conducted in order to get a tertiary comparison with the experimental results, and to provide an estimate of the unsteady lift and drag coefficients, which were not readily obtainable in the experiments. The images were processed on ANSYS CFD-Post.

3.1 Simulation methodology

The two-dimensional system was designed in the SolidWorks computer-aided-drafting (CAD) software to replicate the wind tunnel geometry. Again, the airfoil tested in the current study, was a NACA 0012, which was fixed at 0° local angle relative to rotational circle at the airfoil's quarter-chord position. The airfoil was located at a radial location of 0.17 m (6.5 in) from the center of rotation on a rotating, circular domain which was 0.21 m (8.2 in) in radius. The resulting geometry was a planar domain, with a circular shape with the airfoil area subtracted from it at the defined location. The flow domain was 3.3 m in length, extending 7 times, the rotor diameter downstream from the rotor. The processing of the geometry and meshing was carried out in the Workbench Module of ANSYS. The cell size at the airfoil surface and inside the domain was given the priority and sets the basis of the meshing scheme for the system. The y^+ at the airfoil surface was set less than 1 with 4 inflation layers which capture the viscous sub-layer of the boundary layer flow. With a growth rate of 1.15 a significant part of the rotating domain fell under the log-law region. A sample image of the mesh surrounding the airfoil is presented in Figure 3.1, while the equations for y^+ criteria are given below.

$$C_f = 0.026 Re * 1/7$$

$$\tau_w all = C_f U_\infty^2$$

$$U_{fric} = sqrt(\tau_{wall}\rho)$$

$$\Delta s = y + \mu U_{fric}\rho, wallspacing$$

The total number of cells in the circular domain was approximately 2.4×10^6, while in the fixed (non-rotating) domain there were 3.0×10^4. Simulations were carried in FLUENT using several 2-equation RANS turbulence models and an LES model. The moving mesh technique was used to simulate the flow around a single rotating airfoil. The time-step for simulations was chosen to be equivalent to 1° rotation. This value was well below the vortex shedding frequency of the system, and is agreeable with similar simulations carried out in the literature. The pressure-based solver approach is considered under transient state. The pressure-based solvers take momentum and pressure (or pressure correction) as the primary variables. The pressure-velocity coupling algorithms were derived by reformatting the continuity equation. The pressure based
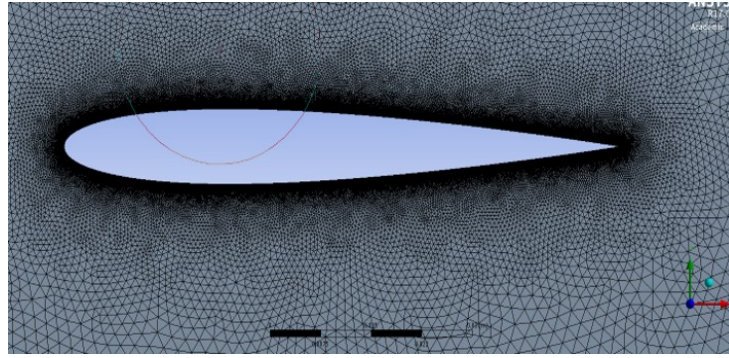
Figure 3.1: Meshing near the airfoil

solver was selected because it is applicable for a wide range of flow regimes, from low speed incompressible flow to high-speed compressible flow. Furthermore, it required less memory (storage) and allowed more flexibility in the solution procedure. The gradients of the solution variables were calculated in the center of the cells. Gradients of the solution variables were required in order to evaluate the diffusive fluxes, the velocity derivatives, and for the higher-order discretization schemes. The Green-Gauss Node-Based approach was used as it is more accurate that the Gauss-Gauss Cell Based approach, minimizes false diffusion, and was recommended for tri/tet cell geometry meshes; eventhough it demands more computational power. The pressure-velocity coupling refers to the numerical algorithm which used a combination of continuity and momentum equations to derive an equation for pressure (or pressure correction) when using the pressure-based solver. The default SIMPLE algorithm is used because of its lower computational cost, where the SIMPLE algorithm uses a relationship between velocity and pressure corrections to enforce mass conservation and obtain the pressure field; eventhough it is not the best suited solver algorithm for this job. A more preferred solver for this unsteady flow would have been the Pressure-Implicit with Splitting of Operators (PISO). The pressure was evaluated using the PRESTO scheme. This is done as this model is preferred for highly swirling flows, flows involving steep pressure gradients (porous media, fan models, etc.), or in strongly curved domains. Since the model represented a rotating system with high tip speed, PRESTO represented an ideal option for the present study. The interpolation scheme for the momentum equation, turbulent kinetic energy, and dissipation rate was chosen to be second-order rather than QUICK (Quadratic Upwind Interpolation.) Although, QUICK discretization scheme may provide better accuracy than the second-order

scheme for rotating or swirling flows solved on quadrilateral or hexahedral meshes, for general cases it does not provide much of a benefit over a Second Order Upwind scheme [10].

3.1.1   Turbulence Models

Two turbulence models where utilized and compared for the URANS simulations in the current study. Both of the models are discussed in detail below.

The Realizable k-ϵ Model   was proposed in [36]. The term "realizable" implies that the model satisfies certain mathematical constraints on the normal stresses, consistent with the physics of turbulent flows. In the calculation of high-gradient streams, negative values of eddy viscosity are excluded. An improvement method for calculating the turbulent viscosity was introduced in this model and the equation for the dissipation rate was derived from the exact transport equation for the fluctuating component of the vorticity. Compared to the standard version of the k-ϵ model, the "realizable" model more accurately predicts the distribution of the dissipation rate of the flat and round jets and has been shown to provide a better prediction of the boundary layer characteristics in large pressure gradients, separated regions, and recirculating flows.

Note, the equations for the realizable k-ϵ model are presented below.

$$\frac{\partial}{\partial t}(\rho k) + \frac{\partial}{\partial x_j}(\rho k u_j) = \frac{\partial}{\partial x_j}\left[\left(\mu + \frac{\mu_t}{\sigma_k}\right)\frac{\partial k}{\partial x_j}\right] + P_k + P_b - \rho\epsilon - Y_M + S_k$$

$$\frac{\partial}{\partial t}(\rho\epsilon) + \frac{\partial}{\partial x_j}(\rho\epsilon u_j) = \frac{\partial}{\partial x_j}\left[\left(\mu + \frac{\mu_t}{\sigma_\epsilon}\right)\frac{\partial\epsilon}{\partial x_j}\right] + \rho\, C_1 S\epsilon - \rho\, C_2 \frac{\epsilon^2}{k+\sqrt{\nu\epsilon}} + C_{1\epsilon}\frac{\epsilon}{k}C_{3\epsilon}P_b + S_\epsilon$$

where

$$C_1 = \max\left[0.43, \frac{\eta}{\eta + 5}\right], \quad \eta = S\frac{k}{\epsilon}, \quad S = \sqrt{2S_{ij}S_{ij}}$$

In these equations, P_k represents the generation of turbulent kinetic energy due to the mean velocity gradients, calculated in same manner as standard k-ϵ model. P_b is the generation of turbulent kinetic energy due to buoyancy, calculated in same way as standard k-ϵ model.

The turbulent viscosity is modeled as

$$\mu_t = \rho C_\mu \frac{k^2}{\epsilon}$$

where

$$C_\mu = \frac{1}{A_0 + A_s \frac{kU^*}{\epsilon}}$$

$$U^* \equiv \sqrt{S_{ij}S_{ij} + \tilde{\Omega}_{ij}\tilde{\Omega}_{ij}}$$

$$\tilde{\Omega}_{ij} = \Omega_{ij} - 2\epsilon_{ijk}\omega_k$$

$$\Omega_{ij} = \overline{\Omega_{ij}} - \epsilon_{ijk}\omega_k$$

and Ω_{ij} is the mean rate-of-rotation tensor viewed in a rotating reference frame with the angular velocity ω_k. The model constants A_0 and A_s are given by: $A_0 = 4.04$, $\quad A_s = \sqrt{6}\cos\phi$ $\phi = \frac{1}{3}\cos^{-1}(\sqrt{6}W)$, $W = \frac{S_{ij}S_{jk}S_{ki}}{\tilde{S}^3}$, $\quad \tilde{S} = \sqrt{S_{ij}S_{ij}}$, $\quad S_{ij} = \frac{1}{2}\left(\frac{\partial u_j}{\partial x_i} + \frac{\partial u_i}{\partial x_j}\right)$ The realizable model was unable to satisfactorily predict the radial velocity. It was also the most computationally-expensive model tested in the current study [28].

The SST k-ω Model is reputed to be more accurate than the k-ϵ model in the near-wall layer [6]. It has been successfully applied in flows with moderate adverse pressure gradients, but it has an ω equation which is very sensitive to the values of ω in the free stream. The shear-stress transport (SST) term corrects this problem by solving the standard k-ϵ equation in the far field and the standard k-ω equation near the walls [39]. To improve its performance for adverse pressure gradient flows, the SST term considers the effects of the transport of the turbulent shear stress in the calculations of the turbulent viscosity μ_t and the turbulent Prandtl numbers σ_k and σ_ω. The transport equation for k and the specific dissipation rate ω are the following [34]:

$$\frac{\partial(\rho k)}{\partial t} + \frac{\partial(\rho u_j k)}{\partial x_j} = \rho P - \beta^* \rho \omega k + \frac{\partial}{\partial x_j}\left[(\mu + \sigma_k \mu_t)\frac{\partial k}{\partial x_j}\right]$$

$$\frac{\partial(\rho\omega)}{\partial t} + \frac{\partial(\rho u_j \omega)}{\partial x_j} = \frac{\gamma}{\nu_t}P - \beta\rho\omega^2 + \frac{\partial}{\partial x_j}\left[(\mu + \sigma_\omega \mu_t)\frac{\partial\omega}{\partial x_j}\right] + 2(1 - F_1)\frac{\rho\sigma_{\omega 2}}{\omega}\frac{\partial k}{\partial x_j}\frac{\partial\omega}{\partial x_j}$$

where

$$P = \tau_{ij}\frac{\partial u_i}{\partial x_j}$$

$$\tau_{ij} = \mu_t\left(2S_{ij} - \frac{2}{3}\frac{\partial u_k}{\partial x_k}\delta_{ij}\right) - \frac{2}{3}\rho k\delta_{ij}$$

$$S_{ij} = \frac{1}{2}\left(\frac{\partial u_i}{\partial x_j} + \frac{\partial u_j}{\partial x_i}\right)$$

$$\mu_t = \frac{\rho a_1 k}{\max(a_1\omega, \Omega F_2)}$$

$$\phi = F_1\phi_1 + (1 - F_1)\phi_2$$

$$F_1 = \tanh\left(\text{arg}_1^4\right)$$

$$\text{arg}_1 = \min\left[\max\left(\frac{\sqrt{k}}{\beta^*\omega d}, \frac{500\nu}{d^2\omega}\right), \frac{4\rho\sigma_{\omega 2}k}{\text{CD}_{k\omega}d^2}\right]$$

$$\text{CD}_{k\omega} = \max\left(2\rho\sigma_{\omega 2}\frac{1}{\omega}\frac{\partial k}{\partial x_j}\frac{\partial \omega}{\partial x_j}, 10^{-20}\right)$$

$$F_2 = \tanh\left(\text{arg}_2^2\right)$$

$$\text{arg}_2 = \max\left(2\frac{\sqrt{k}}{\beta^*\omega d}, \frac{500\nu}{d^2\omega}\right)$$

The model is less sensitive to the free stream conditions than other turbulence models. The shear stress limiter helps the k-ω model avoid a build-up of excessive turbulent kinetic energy near stagnation points. The SST models provide a platform for additional extensions such as SAS and laminar-to-turbulent transition-[3].

Chapter 4

Experimental Setup

The experimental study primarily depended upon the two-dimensional particle image velocimetry (PIV) method to capture the velocity fields around the cycloidally rotating blade. PIV is a non-intrusive flow diagnostic technique allowing flow field measurements. Comparing with intrusive flow measurement techniques like hot wire anemometry or pressure probes, PIV eliminates the need of instrumental intrusions by using non-intrusive laser light and tracer particles. It can capture large fields with even small fluctuations in a short time [46]. As a result, PIV represented a perfect tool for studying the dynamic stall behavior in the current experiments. A commercial PIV system from LaVision was utilized in the current experiments consisting four main components: the seeding device, the laser light source (used to illuminate the particles), the cameras (used to visually capture the illuminated tracers particles) and the software (used to post-process the image data).

Seeding Generator: Since the flow through the open jet wind tunnel will be transparent, seeding is needed to visualize the flow. For this purpose a Concept II smoke generator was used to produce an oil-based, non-toxic fog in the wind tunnel. The mean particle particle diameter produced by the smoke generator was $\mathcal{O}(1\mu m)$. Tracer particles must be small enough to faithfully follow the fluid motion, while the size of the tracer particles must also be large enough to scatter adequate light to the cameras. Small particles are excellent flow tracers (due to low mass inertia), but may not scatter enough light due to their limited size. For the $\mathcal{O}(1\mu m)$ particles used in PIV measurements, the light scattering is expected to occur in Mie scattering regime, where the particle diameter is comparable or larger than the laser wavelength. In this regime, the strongest scattering occurs at $0°$ and $180°$ with respect to the incoming light angle, while

the weakest scattering concentrates in the direction normal laser direction.

Laser: A bright light source is required for the PIV experiments inorder to illuminate the particles generated by the seeding device. In practical a 200 mJ Quantel Evergreen NdYAG laser was used. The laser power and timing was digitally controlled through the DaVis Software as part of the LaVision system. The pulse duration of the laser was approximately 8 ns with a maximum repetition rate of 15 Hz. Finally, the laser timing was digitally controlled through a LaVision PTUX programable timing unit, to ensure accurate triggering of both the laser and the cameras.

Digital Cameras: The illuminated particles were visually captured by two 5 megapixel LaVision sCMOS cameras, which had a spatial resolution of 2560 by 2160 pixels, a pixel size of 6.5 μm square, a 16 bit dynamic range, and a maximum sampling frequency of 100 Hz. Two Nikon f = 60 mm micro lenses were used with the cameras, providing an approximate field of view of of $\mathcal{O}(1.2R)$.

PIV Post-Processing Software: The DaVis 8.3 software from LaVision, GMBH was used to perform the post-processing of the PIV images. A multipass, fast-Fourier based cross-correlation method was implemented with decreasing interrogation window size. Specifically, four passes were implemented starting with an initial interrogation window size of 64 x 64 pixels and finishing with an interrogation window size of 32 x 32 pixels with 50% overlap between the windows.

Wind Tunnel: The CU Low-Speed, Research Wind Tunnel installed in the Experimental Aerodynamics Laboratory at University of Colorado Boulder was used for the current experiments. The tunnel is an open-return, blow-down configuration built by Aerolab LLC, and uses a belt driven centrifugal fan to drive the flow. The cycloidal rotor model was tested in the the test section which has a 0.76 m x 0.76 m (30 in by 30 in) cross-section and a length 3.6 m (141 in). The wind tunnel can achieve speeds upto 75 m/s.

4.1   Cycloidal Rotor Configuration

A schematic of the setup is shown in Figure 4.1. The cycloidal rotor system was mounted in the center of the wind tunnel with its axis of rotation pointing vertically upwards into the wind tunnel and horizontally centered between the wind tunnel side-walls. The system was designed with a single, rectangular NACA 0012 airfoil blade with a chord of $c = 82.55$ mm (3.25 in) and an aspect ratio of $AR = 1.54$. A single blade rotor
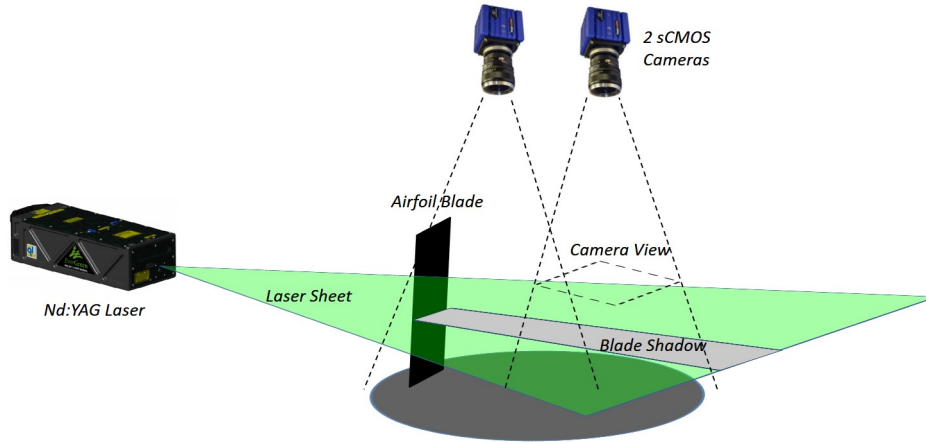
Figure 4.1: Schematic of the experimental setup

was studied to provide a simplified flow interaction, namely limiting the blade vortex interaction and wake shedding inside the rotor space. The rotor had a radius $R = 165.1$ mm (6.5 in) and a solidity is 0.16. The rotor was tested at various wind tunnel and rotor speeds, but limited to three advance ratios which are all detailed in the test matrix presented in Tables 4.1 and 4.2.

The laser for the PIV system was mounted on a traverse outside the wind tunnel and illuminated the rotor disk from the side with the laser sheet oriented in a horizontal plane. It was positioned at the mid-span of the airfoil to mitigate the influence of the three-dimensional flow effects from the wind tunnel boundary layer and blade tip. The two cameras were mounted on a traverse above the camera, and together captured half of the rotor disk in the wind tunnel width direction. Specifically, each camera was positioned to capture a field of view of of $\mathcal{O}(1.2R)$. This was chosen to ensure that the cameras were able to resolve the tracer particles without pixel locking. For the wake measurements, the cameras were positioned to view the wake starting at $\Delta x = 1.5$ in downstream from the rotor disk to avoid laser reflections from airfoil from influencing the measurements. For the measurements captured inside the rotor disk, the cameras were first positioned to capture the flow in the upstream half of the rotor disk ($0° < \theta < 180°$) before being re-positioned to capture the flow in downstream half ($180° < \theta < 360°$). The resulting vector fields were then stitched together during the post-processing of the data to produced a complete view of the rotor disk. However, using a single light source on one side of the system caused the laser to leave a shadow of the
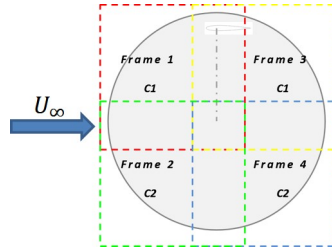
Figure 4.2: Schematic showing the captured frames using 2 cameras

airfoil, which resulted in missing pieces of data in the system, especially at phase angles of $90° < \theta < 270°$ where the blade was closest to the laser source. To overcome this, a second complete set of data collected using the same setup, but with the blade in the reverse direction. So, instead of four frames, a complete set of data consisted of eight frames to form a complete image of the rotor disk. Additional details associated with the post-processing of the data are provided in the following section. The schematic in Figure 4.2 displays how the frames were captured and stitched together using only two cameras. Figure 4.3 displays a graphical example procedure for processing the PIV vector fields. This includes capturing frames, using a mask where the vector calculation is not intended (covering the airfoil and shadow), and then computing the instantaneous velocity field based on pixel intensity shift evaluation.

4.1.1 PIV and testing

The PIV system requires the coupling of the cameras, the laser, and a trigger source to capture the images at desired phase angles. As briefly, discussed in the manufacturing section, an electrical trigger system was designed and constructed to produce a trigger signal for the PIV system. The cameras and laser were then timed through the DaVis software based upon input trigger signal and "reference time" or delay-time to precisely set the desired phase location. Note the trigger system produced a TTL pulse once per cycle at the $\theta = 0°$ phase angle (when the airfoil chord is parallel to the free stream velocity with flow hitting at the airfoil leading edge), and PIV data was collected at every $\Delta\theta = 30°$.

The cameras were calibrated using the the two camera stereo method in DaVis with a three-dimensional type 204-15 LaVision calibration target. Two different coordinate systems were used, one for each camera and the orientation of the coordinate systems were set in the right handed reference frame. During the
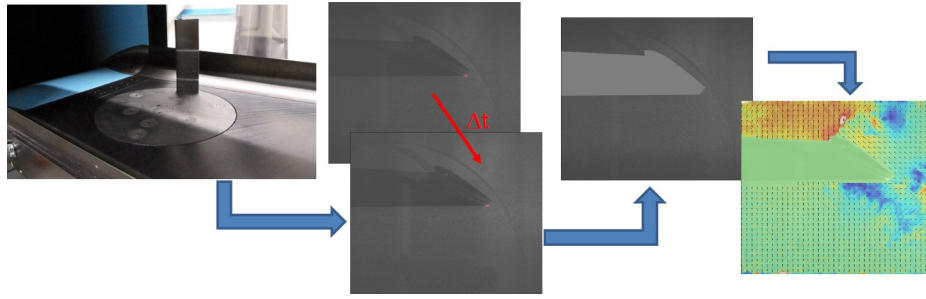
Figure 4.3: Sequence of steps for Image Processing to get the instantaneous vector field

calibration, a known point/dot from the calibration plate was selected at the center of each image/frame as the reference point (not the center of the calibration plate and not the same physical dot in each frame). The software detects all the points on the calibration plate using a 'pinhole' model, which is used when only a portion of image is covered with the calibration target, and creates a grid. The final calibration had an average deviation of the dewarped mark positions less than 0.5 pixels, which was deemed within acceptable limits. Once the calibration was completed the actual desired origin of the complete view was defined for image/vector stitching. This was done in the "Define Origin, Maintain Calibration" section by selecting the dot chosen previously for the second camera and defining its relative, physical position to the dot chosen for the first camera. Two hundred images were then collected for each phase location, for data inside the rotor, and one hundred images were collected for each set in the rotor downstream wake. These sample sizes produced converged phase-averaged velocity fields for the unsteady flow inside the rotor. Finally, prior to performing the PIV processing geometric Masks were defined for each camera, to limit the processing of PIV results in regions were the laser light was shadow by the blade and near the blade surface where bright reflections occurred.

The the sequential cross-correlation PIV processing method was used with a final interrogation window of 32 x 32 pixels, and multi-pass processing. The vector field was merged in the DaVis software for the data behind the rotor. For data inside the rotor, the image processing was more complicated, so the velocity vector fields were instead stitched together in Matlab. The average vector field was calculated from each image set for all 200 images in the set. The four frames from the counter-clockwise rotating system were also stitched together, and the data was then interpolated with the clockwise rotating system data using
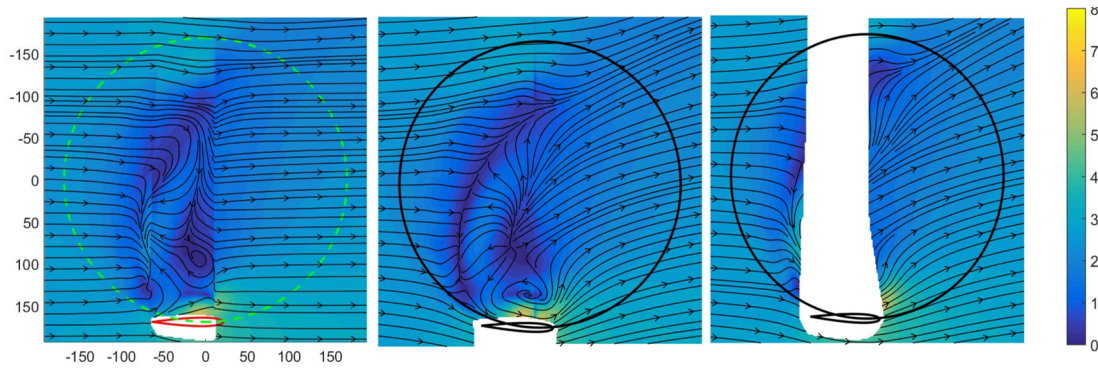
Figure 4.4: (a) Integrated image with anomaly, (b) counter-clockwise rotating case, (c) clockwise rotating case

the 'griddata.mat' function with a 'cubic interpolation' method in Matlab. The origin in the rotor reference frame was defined in each frame, and then the vector fields were shifted on this reference rotor-coordinate system. An attempt was made to rotate the set of images by 180 degrees to mimic the counter-clockwise case, and overlap with the original counter-clockwise case to fill in the missing data in the blade shadow. For this overlap the data was borrowed from one data set to fill in the missing data in the other set by comparing the Masked regions in both the sets. Note, the final data orientation had the airfoil rotating in counter-clockwise direction. All that said the final frames did not exactly overlap well with each other. Even the slightest of misalignment produced large anomalies in the final image resulting into discontinuous data frame. An extreme case of this anomaly is shown in Figure 4.4. Finally, it was realized that data made more sense if individual cases (i.e either clockwise or counter-clockwise) were used to present the results. This final data set was then used to analyze the velocity contours, vorticity, and streamlines.

4.2   Test Matrix

The experiments were carried out for a variety of free stream velocities and rotational speeds to produce three distinct advance ratios $\mu = 0.75$, 1, and 1.25. For flow measurements in the downstream wake 11 cases were tested. For the flow inside the rotor, the system was tested for only one rotational speed at three different free stream velocities, producing a total of 3 cases. These 3 cases were also simulated in CFD using the both the realizable k-ϵ, SST k-ω, and k-ω turbulence models.

Advance Ratio $\frac{U_{\text{inf}}}{\omega r}$	Free-stream Velocity (m/s)	Rotational Frequency (Hz)
1	1.04	1
1.25	1.30	1
0.75	1.56	2
1	2.07	2
1.25	2.5	2
0.75	3.11	4
1	4.15	4
1.25	5.19	4
0.75	3.89	5
1	5.19	5
1.25	6.48	5

Table 4.1: Test Matrix for the flow measurements in the rotor wake.

Advance Ratio $\frac{U_{\text{inf}}}{\omega r}$	Free-stream Velocity (m/s)	Rotational Frequency (Hz)
0.75	3.11	4
1	4.15	4
1.25	5.19	4

Table 4.2: Test Matrix for the flow inside the rotor and in the CFD simulations.

Chapter 5

Results and Discussion

The flow around a cycloidal rotor is highly unsteady and complex. This makes the quantitative and qualitative study of system extremely challenging. The effects of these unsteady flow conditions will be apparent in the following analysis. The complexity of the flow not only makes the cycloidal rotor flow dynamics unique, but also shows fundamental differences when comparing results between the computational and experimental data.

The general dynamics of a cycloidal rotor can be summarized in four sections of the system, (1) the windward section ($315° < \theta < 45°$): where the airfoil encounters the maximum flow velocity at minimum angle of attack, (2) the upwind section ($45° < \theta < 135°$): the airfoil undergoes dynamic stall, (3) the leeward section ($135° < \theta < 225°$): the airfoil sheds the vortex pair as it approaches minimum local velocity with highly unsteady flow, (4) the downwind section ($225° < \theta < 315°$): the airfoil interacts with its own wake/vortices. However, the phenomena observed in these regions can shift on the operating parameters. This phenomenon can be seen in Figure 5.1. The analysis of these phase averaged flow fields for different cases of advance ratio shows some fundamental differences in the dynamics of the system.

Figure 5.2 shows a comparison between the phase-averaged velocity for the flow downstream from the rotor at three different advance ratios. Where the velocity is non-dimensionalized by the free stream velocity. The x-axis shows the length in rotor reference frame, where $x = 0$ mm is the center of the rotor and rotor diameter is 165.1 mm. It can be seen that the velocity profiles are similar for the same advance ratio cases. This can also be seen by comparing the vorticity contour plots for the flow exiting the rotor at all phases operating at the same advance ratios. This is shown in Figures 5.3, 5.4, and 5.5.

(1) Windward: The leading edge is at a positive angle
of attack while the trailing edge is at negative
angle of attack

(2) Upwind: Occurrence of Dynamic Stall with Leading
and Trailing edge vortices

(3) Leeward: Wake shedding from the airfoil

(4) Downwind: Wake-Blade Interaction
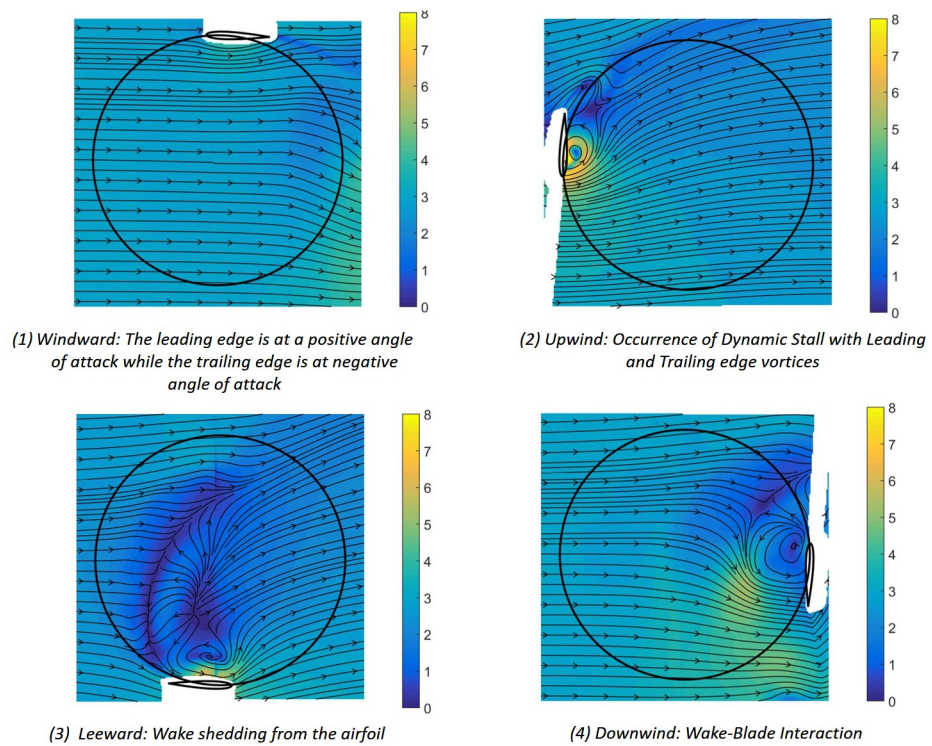
Figure 5.1: Flow Dynamics summarized using four instances from μ=0.75 case
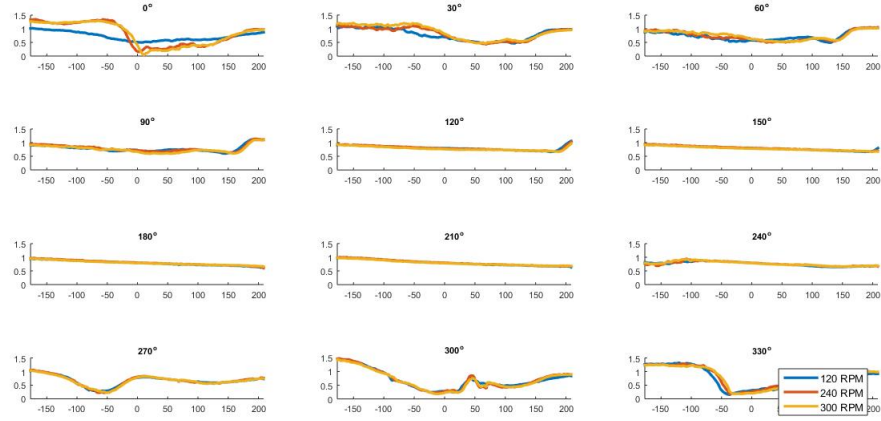
(a) Non-dimensionalized resultant velocity downstream of the rotor at $\mu = 0.75$
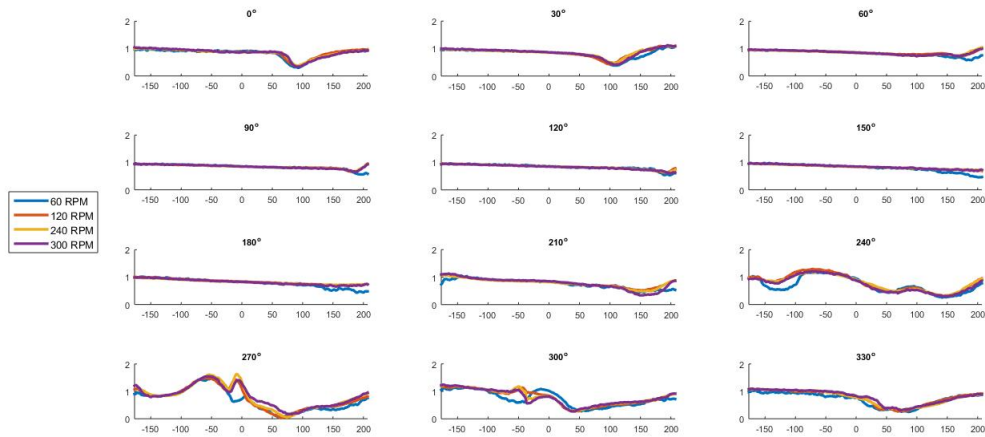
(b) Non-dimensionalized resultant velocity downstream of the rotor at $\mu = 0.75$
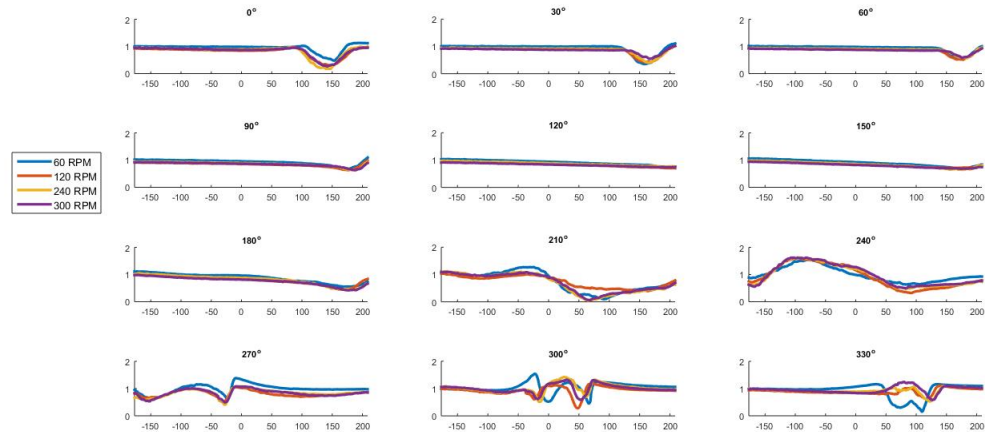
(c) Non-dimensionalized resultant velocity downstream of the rotor at $\mu = 0.75$

Figure 5.2: Comparison of phase averaged results showing the similarity of the flow for different Reynolds numbers at same advance ratios
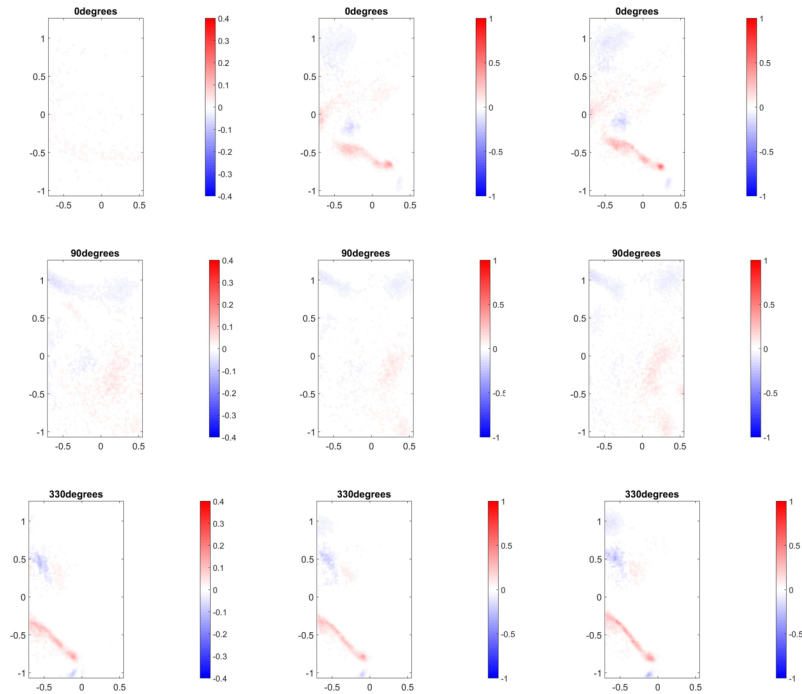
Figure 5.3: Comparison of phase averaged Vorticity Contour downstream of the rotor (μ=0.75) at 120 RPM, 240 RPM, 300 RPM (a) 0 degree (b) 90 degree (c) 330 degree
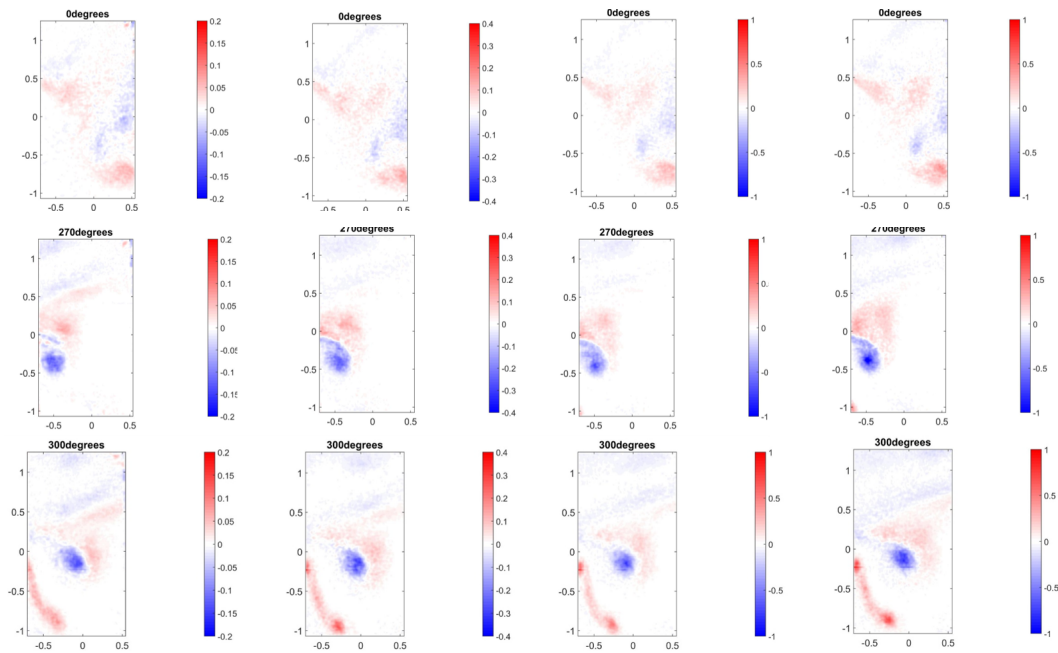
Figure 5.4: Comparison of phase averaged Vorticity Contour downstream of the rotor at 60 RPM, 120 RPM, 240 RPM, 300 RPM (μ=1) (a) 0 degree (b) 270 degree (c) 300 degree
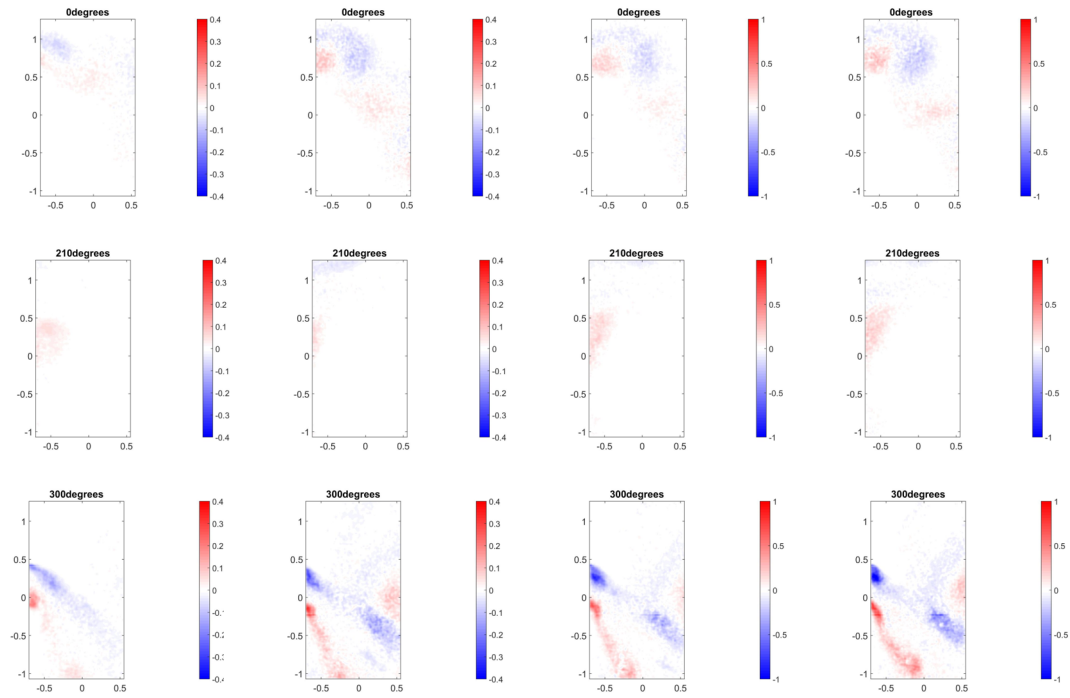
Figure 5.5: Comparison of phase averaged Vorticity Contour downstream of the rotor at 60 RPM, 120 RPM, 240 RPM, 300 RPM (μ=1.25) (a) 0 degree (b) 210 degree (c) 300 degree

As the airfoil revolves around the rotor, the generation of a dynamic stall vortex is observed in each of the three cases, but at slightly different phase angles. As the images are taken at every $\Delta\theta = 30°$, the results do not show the exact location where the leading edge vortex (LEV) is formed or shed. However by comparing the frames for different cases at each phase it is observed that there is a difference in the azimuth location where the LEV occurs. This is shown in Figure 5.6.

The results show that for all three cases dynamic stall occurs between azimuth angles of $30° < \theta < 60°$. But from the velocity contour plots around the airfoil blade it can be seen that for $\mu = 1.25$ dynamic stall occurs much earlier than for $\mu = 1$ and 0.75. Similarly, for $\mu = 1$ dynamic stall occurs earlier than at $\mu = 0.75$. For $\mu = 0.75$, dynamic stall occurs near $\theta = 60°$. At this position the airfoil's local angle of attack at the quarter chord position is $\alpha \approx 34.72°$ and relative velocity is $U_r \approx 6.31\ m/s$. At the same position for an advance ratio of $\mu = 1$, the dynamic stall vortex seems to have matured, indicating that the airfoil undergoes dynamic stall at a position prior to $\theta = 60°$. For $\mu = 1.25$, the dynamic stall vortex has developed to what appears to be its full strength with a strong separation bubble appearing near the leading edge of the airfoil. The effective (local) angles of attack varies by approximately $\Delta\alpha = 4°$ between these three cases at $\theta = 60°$, with local angle of attack largest for the case of $\mu = 1.25$. Additionally, this advance ratio also has the largest rate of change of angle of attack. Combined with the fast rate of change of resultant velocity this leads to an earlier occurrence dynamic stall. Note, that the resultant velocity for this case at the same azimuth position, $\theta = 60°$, is $U_r = 8.10 m/s$.

A better understanding of the position of occurrence of dynamic stall can be gained by observing the velocity contours for a case in this region to the velocity contour at next azimuth location ($\theta = 30°$ and $\theta = 60°$) of the following advance ratios. It is observed that the flow dynamics at an instance for $\mu = 0.75$ is similar to that observed at the previous instance of $\mu = 1.25$. This means that they seem to be about $\Delta\theta = 30°$ apart in phase in the upwind section (Figure 5.8). This comparison is based on the position of LEV on the blade chord. In the leeward section, this lag increases to almost $\Delta\theta = 60°$. Note, the phase angle for the occurrence of dynamic stall cannot be better pin-pointed without further resolving azimuthal position at a higher resolution. The LEV travels along the blade chord and is protected from much of the influence of the free stream in this region. As shown in Figure 5.7, it can be seen that for all three cases
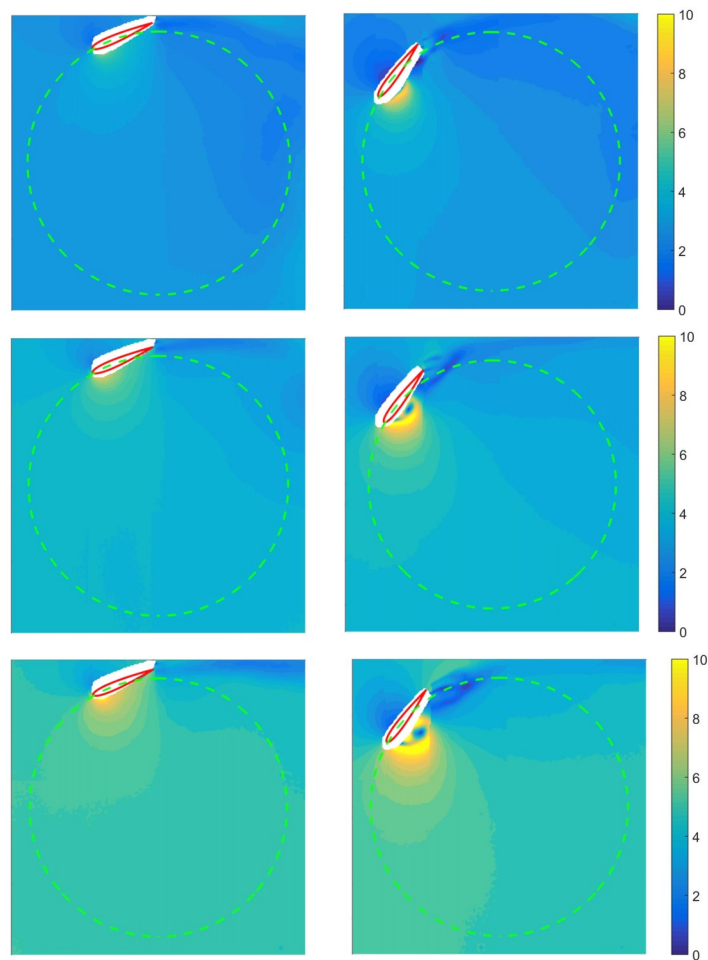
Figure 5.6: Velocity contour in the Rotor when airfoil is at azimuth angles of 30 and 60 deg, showing variation in the occurrence of Dynamic Stall for the three advance ratios at rotor speed of 240 RPM (a) μ=0.75 (b) μ=1 (c) μ=1.25
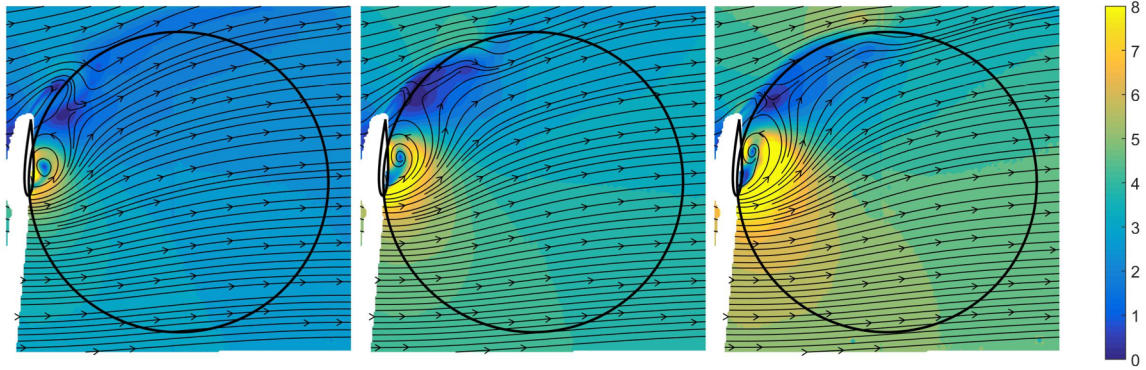
Figure 5.7: Breaking of Dynamic Stall vortex for the three cases μ (1) 0.75 (2) 1 (3) 1.25, at 90 degree azimuth location

the traveling LEV creates a separation bubble on the surface of the airfoil. Also, the wake from the trailing edge is seen to shed from the pressure side of the airfoil which combines with the separation bubble on the suction side between $90° < \theta < 120°$ as shown in Figure 5.15.

As the airfoil crosses the $\theta = 90°$ azimuthal position it translated from an upward to downward flow condition, i.e it starts moving in the retreating side of the flow. The LEV separates from the airfoil as it reaches the trailing edge. After separation, it does not travel freely with the free-stream, but is dragged near the airfoil surface. As the wake is shed from the trailing edge it is dragged along with the airfoil due to the induced rotational velocity by the airfoil. At the same time the free stream pushes the free end of this wake. The result of the superposition of these two effects is stretching of the wake. This is shown in Figure 5.9. This wake is responsible for bending of the flow inside the rotor. As the flow over the airfoil reaches the local minimum velocity the vortex sheds away from the influence of the airfoil, following a curved trajectory. This result is similar to those presented by Tsai & Colonius [39], however they ran the CFD tests at very low advance ratios.

The LEV diffuses quickly in the leeward side of rotation between $150° < \theta < 180°$. At $\theta = 180°$ the airfoil reaches its minimum local flow velocity, and also observes a reversal of the instantaneous angle of attack. This leads the suction side of the airfoil to change to pressure side resulting in the formation of clockwise rotating vorticity at the leading edge and a counter rotating vortex at the trailing edge. This

Figure 5.8: Phase lag between (a) μ=0.75 and (b) μ=1.25 with similar flow conditions

Figure 5.9: Velocity contour for μ=1 showing wake stretching and separation from the trailing edge of the airfoil

result is seen clearly in the CFD simulation as shown in Figure 5.23.
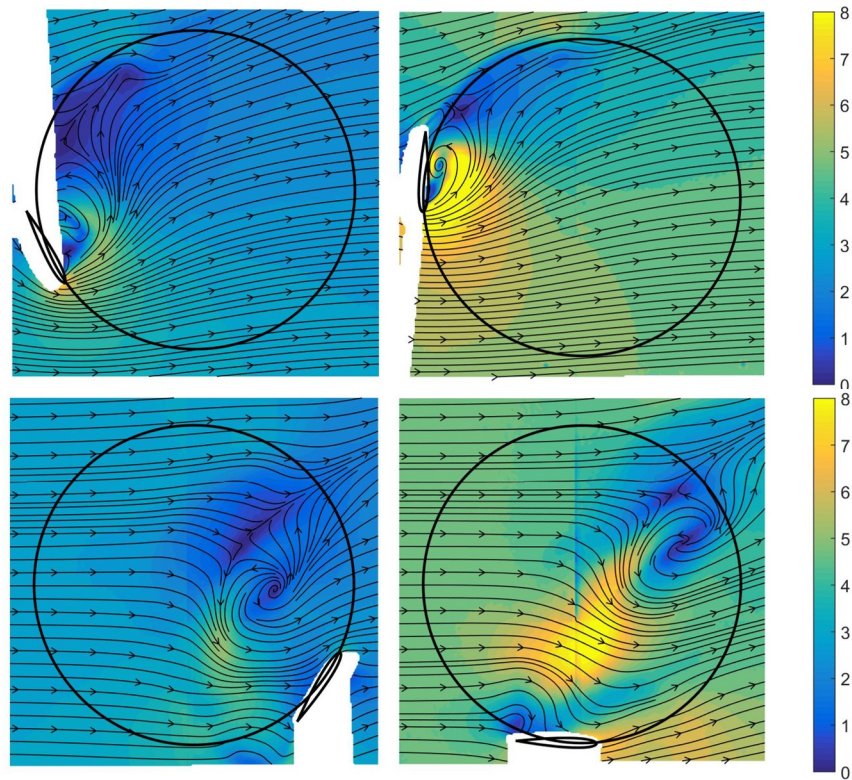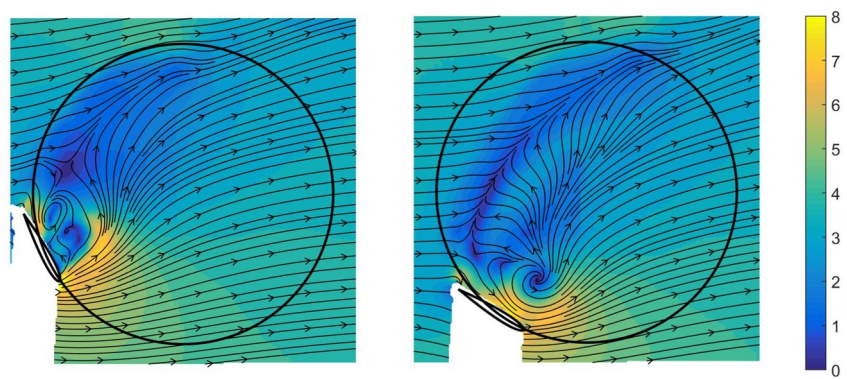
At this point the leading and trailing vortices separate from the airfoil and move downstream along with the free stream, but in different trajectories due to spatial difference in velocity field across the rotor. The LEV induces a localized region of high velocity fluid near the airfoil surface at $\theta = 150°$. This region then advects downstream along with the free stream and is also responsible for pushing the shed LEV in a curved trajectory away from the airfoil. For $\mu = 1.25$, the airfoil encounters this high velocity region as it moves from $\theta = 180°$ to $\theta = 240°$, in front of the airfoil and possibly resulting in increase in torque as shown in Figure 5.10. For $\mu = 1$ a similar behavior is seen, however the airfoil encounters this region head-on at an azimuthal position of $\theta = 240°$ as shown in Figure 5.11. For $\mu = 0.75$, this region of local high velocity fluid moves slowly along with the free stream and does not disturb the airfoil at all as shown in Figure 5.12. These results, obtained from PIV data, are different from what is observed in the CFD results where the airfoil passes through this region of high advective velocity as shown in Figure 5.22. The counter-clockwise rotating vortex does not interact with airfoil for $\mu = 1.25$ and 1, but has a collision with airfoil at $\mu = 0.75$. At $\theta = 270°$ the airfoil leaves a leading edge vortex in all the cases similar to the one left at $\theta = 90°$. However, the strength of the resulting vortex depends on the local velocity of the flow interacting with the airfoil at $\theta = 270°$. This can be seen in Figure 5.13, where the flow behind the rotor shows the shed vortex for the three cases.

By this time the shed wake from the trailing edge during the leeward phase has already passed the rotor boundaries for $\mu = 1.25$, and $\mu = 1$ cases. This happens at $\theta = 210°$ for $\mu = 1.25$, and around $\theta = 240°$ for $\mu=1$. However, for $\mu = 0.75$ the airfoil directly encounters this vortex as it passes between $270° < \theta < 300°$ leaving a turbulent wake behind it as shown in Figure 5.12. This shows the difference in flow dynamics for the cycloidal rotor as the system translates through an advance ratios about $\mu = 1$.

A set of velocity time-history contour plots are shown in Figure 5.14. It shows the propagation of the positive and negative vortex pairs generated by the cycloidal rotor. For $\mu = 1$, the wake shed from the trailing edge at $\theta = 90°$ crosses the rotor when the airfoil is at around $\theta = 240°$. This is seen in the top half of Figure 5.14(b). At $\theta = 270°$ a new vortex pair shed by the airfoil appears at the center of the figure. In the lower half the low velocity region appears which is shed at $\theta = 180°$. The lower intensity is a result
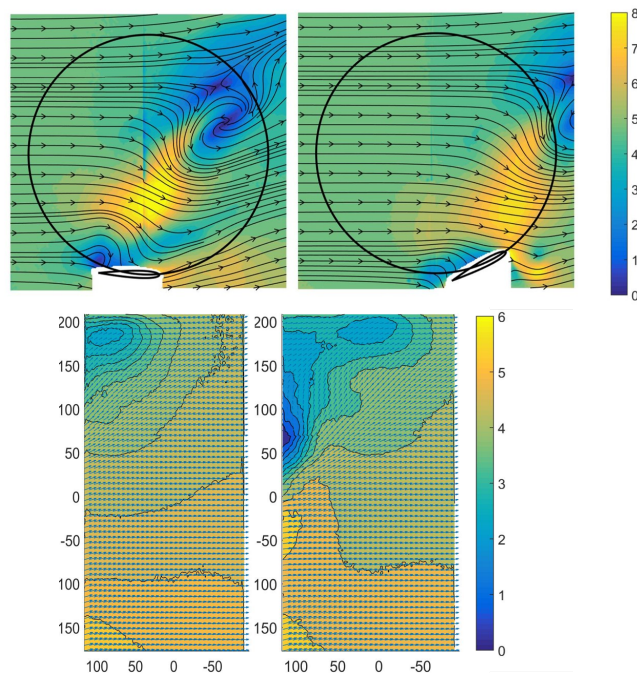
Figure 5.10: Velocity contour for μ=1.25 showing the shed vortex interaction with the airfoil (a) Velocity contour inside the rotor (b) Velocity contour downstream of the rotor at airfoil position of 180 and 210 degrees

Figure 5.11: Velocity contour for μ=1 showing the shed vortex interaction with the airfoil (a) Velocity contour inside the rotor (b) Velocity contour downstream of the rotor at airfoil position of 210 and 240 degrees

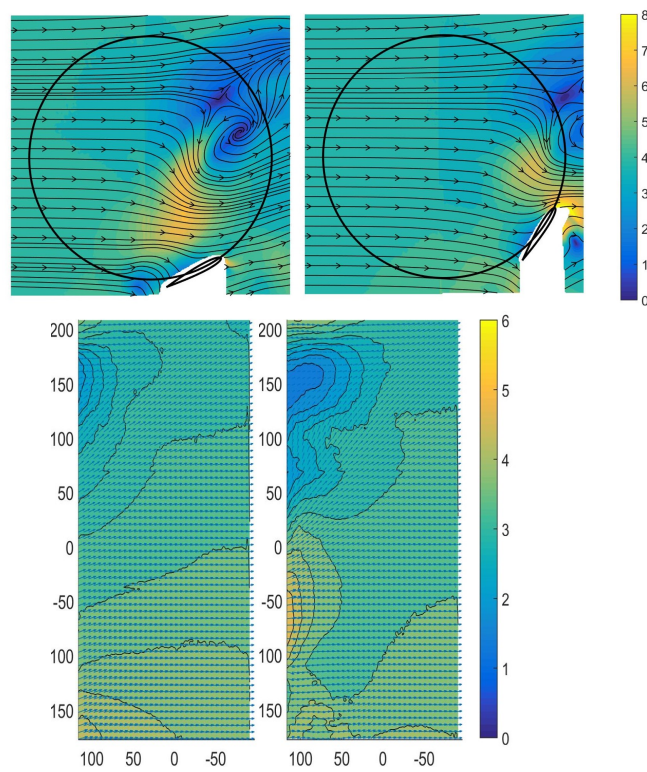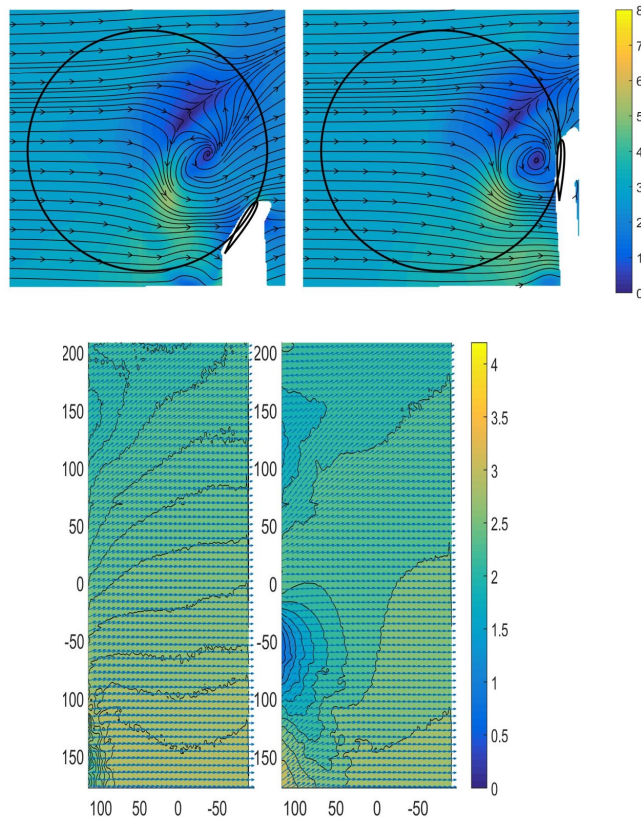Figure 5.12: Velocity contour for μ=0.75 showing the shed vortex interaction with the airfoil
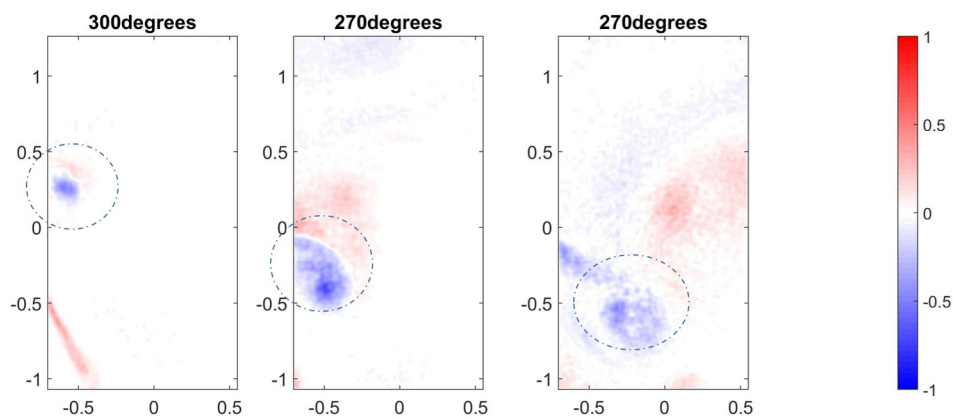

Figure 5.13: Vorticity Contour behind the rotor showing the shed LEV and Wake for (a) μ=0.75 at 300 degree, (b) μ=1 at 270 degree, (c) μ=1.25 at 270 degree

of the airfoil interaction with this region at $\theta = 240°$, which dissipates some of its energy and adds to the vortex pair generated at $\theta = 270°$. It is expected that these two vortex pairs (one shed at $\theta = 90°$ and other at $\theta = 270°$) will further interact with each other as they leave the vicinity of the rotor. Some of this effect is seen in the velocity contours for $\theta = 300°$ and $330°$. This is an important point to be considered for further study, for applications where cycloidal rotors can make use of vortex enhanced propulsion and also while designing wind farms where the progression of shed vortices becomes critical. A similar phenomenon is observed for $\mu = 1.25$. The only difference is the phases angles at which vortex pairs appear, and an evident stretched wake trajectory for $\mu = 1.25$ as compared to $\mu = 1$ as seen in Figure 5.14(c). For $\mu = 0.75$, the airfoil interacts with the vortex shed at $\theta = 90°$ and does not disturb the high velocity region shed at $\theta = 180°$, which appears much stronger in the lower half of the velocity contours as shown in Figure 5.14(a). Also, since no energy is extracted for it, the LEV generated at $\theta = 270°$ is not very strong. The wake trajectory is in a compact cycloidal motion as compared to the previous two cases.

The coefficients of force calculated using different URANS models are compared with each other and that estimated by the potential flow theory in Figure 5.16. The coefficients are obtained by normalizing the forces by dynamic pressure using free stream velocity and chord length ($c_l = \frac{L}{0.5 * \rho * c * (U_{\text{inf}})^2}$).

The system produces a net force in both thrust and lift directions. This is due to the curvature effect of the flow. In the upwind side of the rotor the airfoil encounters a head on free stream velocity, while in the downwind section it sees retreating flow. Secondly, the local angle of attack as seen by the airfoil changes direction from negative to positive as it translates half way between the upwind and downwind sections. This overlap of changing local velocity and local angle-of-attack results in a complex force distribution as the airfoil rotates around the rotor. Figure 5.17 shows the coefficient of lift and drag variation against the blade azimuth position for the resolved forces in the Y and X directions respectively of the rotor for an advance ratio of 1.25. The results show that the SST k-omega model predicts the maximum drag of all the models, experienced by the airfoil at $\theta = 90°$ followed by the Realizable k-ϵ model. This is due to an exaggerated prediction of turbulence by the Realizable k-ϵ and SST models in the regions of high acceleration and stagnation. The potential flow model does not consider the wake generation and separation which is a critical part of the cycloidal rotor fluid dynamics. The k-ω model results are very close to the potential flow

330 ° | 300 ° | 270 ° |240 ° | 210 ° | 180 ° | 150 ° | 120 ° | 90 ° | 60 ° | 30 ° | 0 °

330 ° | 300 ° | 270 ° |240 ° | 210 ° | 180 ° | 150 ° | 120 ° | 90 ° | 60 ° | 30 ° | 0 °

330 ° | 300 ° | 270 ° |240 ° | 210 ° | 180 ° | 150 ° | 120 ° | 90 ° | 60 ° | 30 ° | 0 °
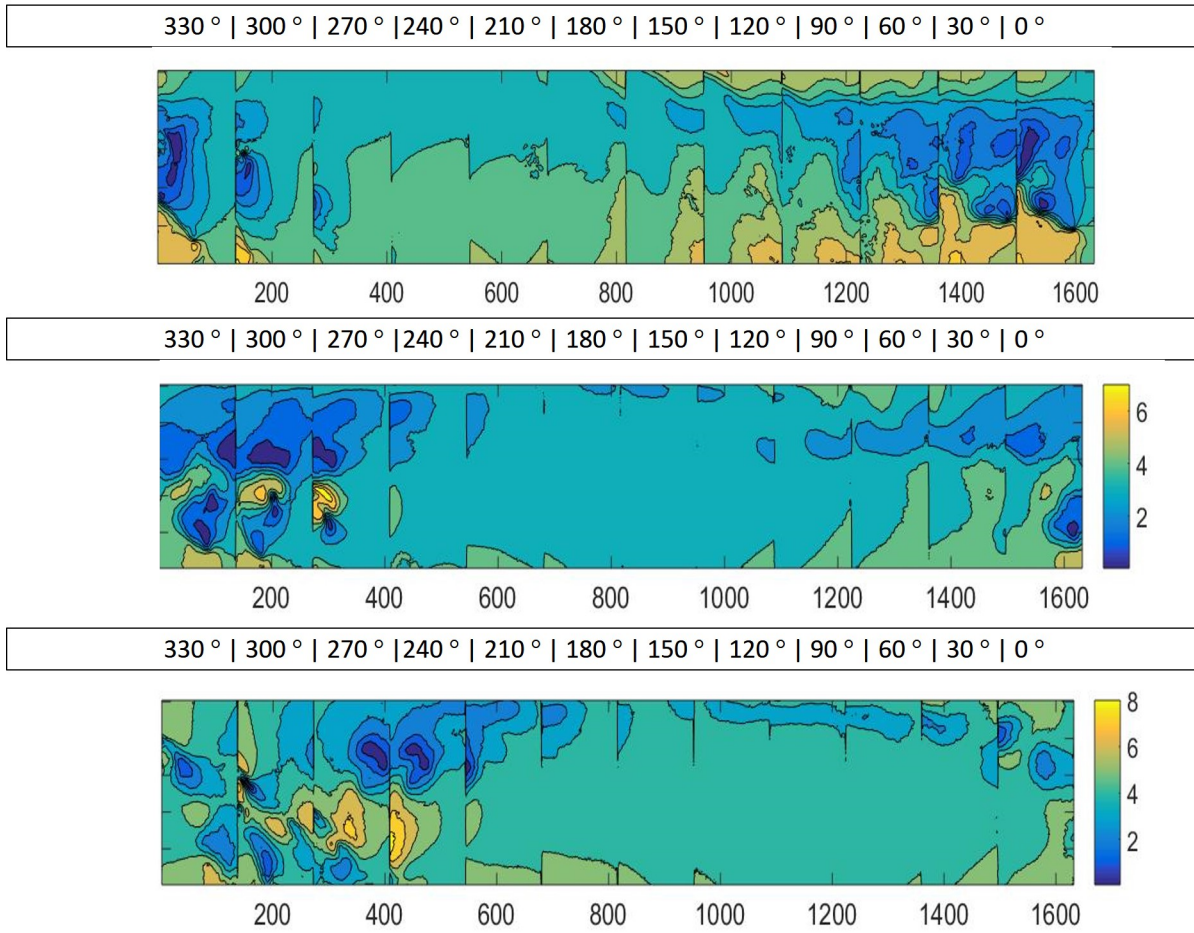
Figure 5.14: Wake Propagation shown by the time history velocity contours behind the rotor (a) μ=0.75 (b) μ=1 (c) μ=1.25
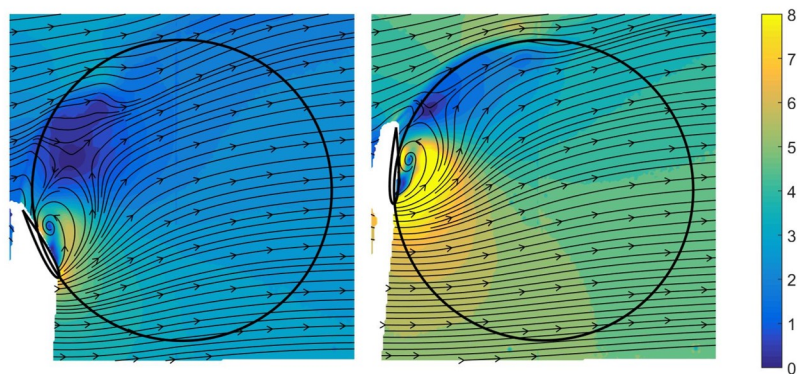
Figure 5.15: Velocity Contour plots at 2 different instances showing the wake and separation bubble joining together (a)μ=0.75 (b) μ=1.25
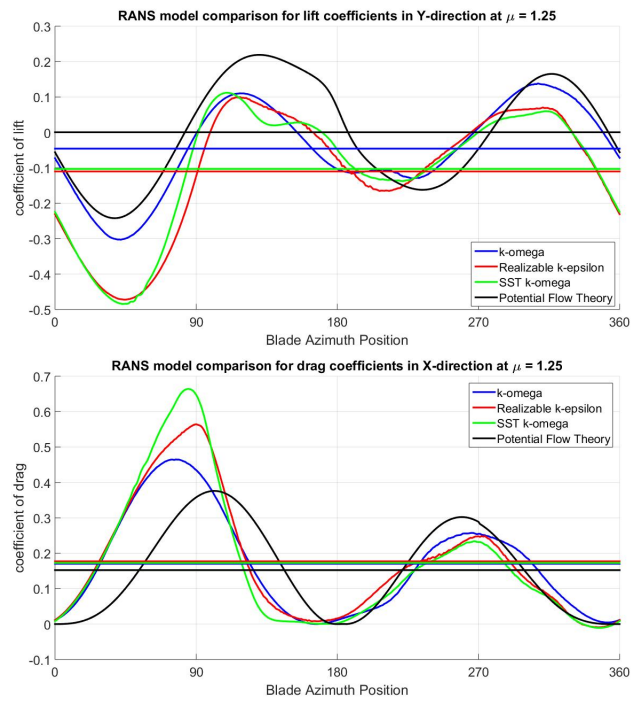
Figure 5.16: (a) Coefficient of lift for different turbulence models for μ=1.25 (b) Coefficient of drag for different turbulence models for μ=1.25

model in the first half of the rotation ($0° < \theta < 180°$). This model under predicts the separated flow. All the models predict the maximum peaks at slightly different azimuth positions. Also, a slight fluctuation in drag is observed between $210° < \theta < 240°$. This is due to the interaction of the airfoil with the shed vortex in this region. However, the average coefficient of drag is nearly the same. Figure 5.17 shows the comparison between the coefficients of force for different advance ratios using SST k-ω model. The difference in peaks of the cyclic change in drag and lift curves decrease as the advance ratio increases. The system produces more lift force for $\mu = 0.75$ as compared to $\mu = 1.25$, but also produces more drag force. Figure 5.18 shows the drag polar plot for the three advance ratio cases.

A qualitative analysis between the CFD and experimental results show reasonable similarity for realizable k-ϵ and SST models. The k-ω model predicts the formation of separation bubble accurately. The models accurately capture the dynamic stall phenomenon Figure 5.19. The advection of shed vortex, however, show some differences between the experimental and computational results. There is not much of a difference between results from realizable k-ϵ and SST models, however realizable k-ϵ seems to perform better both near and far from the walls (Figures 5.19 and 5.20). Also, in a highly unsteady region (in leeward section) the k-ω model performs much better than the other two models. This is seen in Figure 5.21 where the flow appears very different in all the models and k-ω model provides the closest similarity to the PIV result.

Figure 5.22 shows the flow at $\theta = 90°$ comparing the results from PIV and CFD SST model. It shows the velocity and vorticity contours depicting the LEV and TEV. Figure 5.23 shows the vortex formation on the airfoil as it is rotates from $90° < \theta < 210°$ (This image was processed on Tecplot 360). The LEV and TEV dissipates quickly and is dragged with the airfoil. There is reversal of vortex polarity at $\theta = 180°$ where the LEV separates and advects downstream. Similar phenomenon was observed above in experimental results but at different phase angles. This difference can be either due to the difference in 3-D and 2-D vortex dynamics, or due to difference in behavior of turbulence models at different flow conditions.

The trajectory of the shed dynamic vortex is estimated by observing the phase averaged results. Due to the superposition of the free steam and rotational velocity the shed dynamic stall vortices follow different trajectories in all three cases, and this determines whether the blade will encounter the wake in its path. Figures 5.24, 5.25, and 5.26 show the propagation of LEV, and other elements of rotor dynamics at all twelve
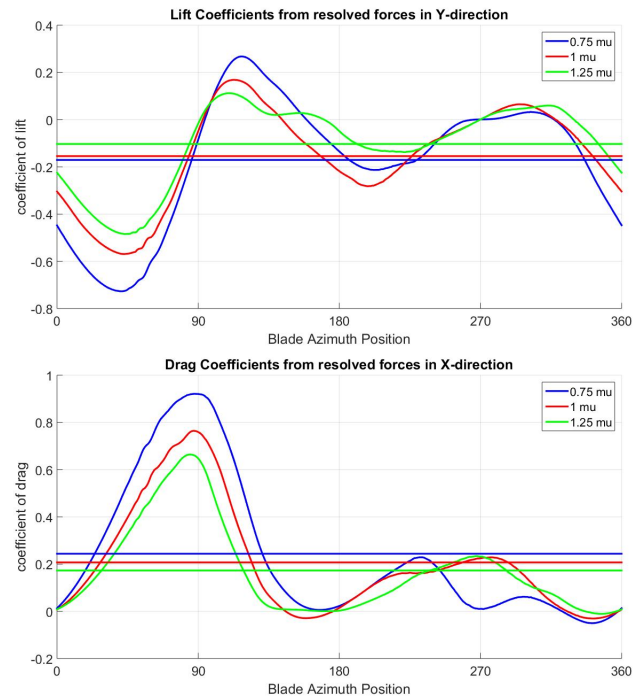
Figure 5.17: (a) Coefficient of lift for different values of μ (b) Coefficient of drag for different values of μ
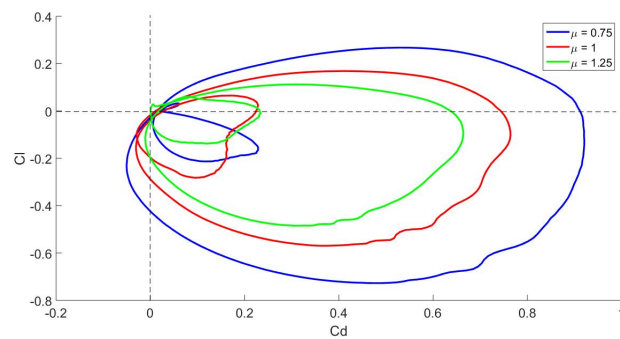
Figure 5.18: Drag Polar plots for the three cases of advance ratio

(a) Velocity Contours from 3 Turbulence
models. SST k-Omega and Realizable
k-epsilon models predict the flow
more closely as compared to
Standard k-Omega model.

Realizable k-epsilon

Standard k-Omega

SST k-Omega

(b) PIV Velocity contour showing the
detachment of Dynamic Stall LEV and
shedding of TEV.
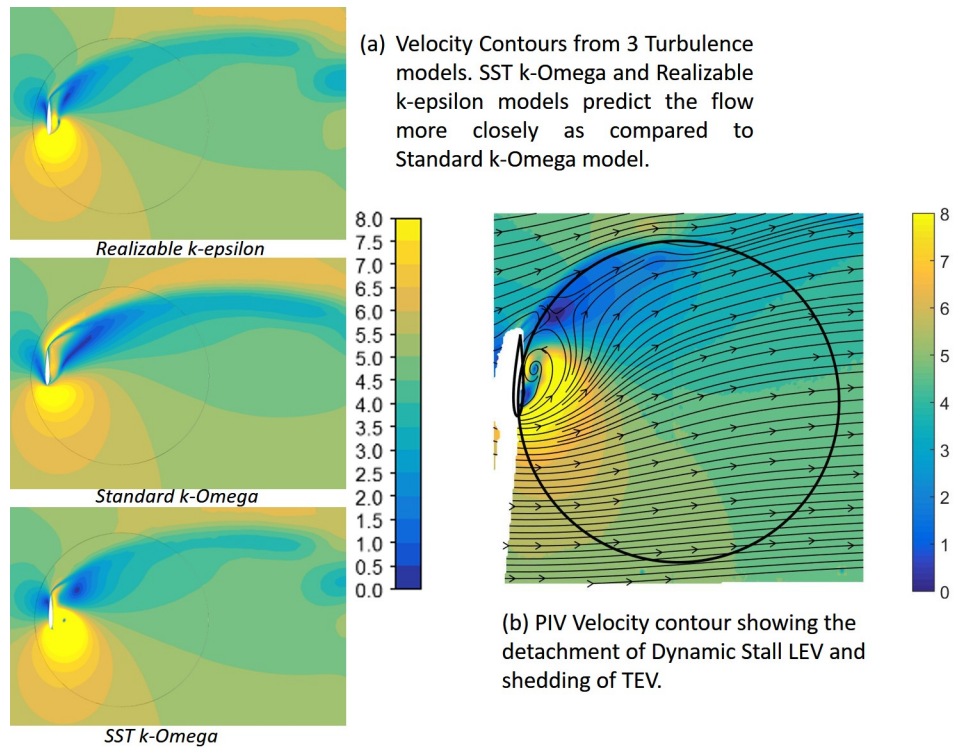
Figure 5.19: Comparison between different models and PIV data at 90 degree $\mu = 1.25$

(a) Velocity Contours from the 3
Turbulence models. The Realizable k-
epsilon and SST k-omega models show
similar flow dynamics, which is
significantly different from the shown
by Standard k-Omega model.

Realizable k-epsilon

Standard k-Omega

SST k-Omega

(b) PIV Velocity contours showing
breaking of separation bubble and
shedding of the vortex.
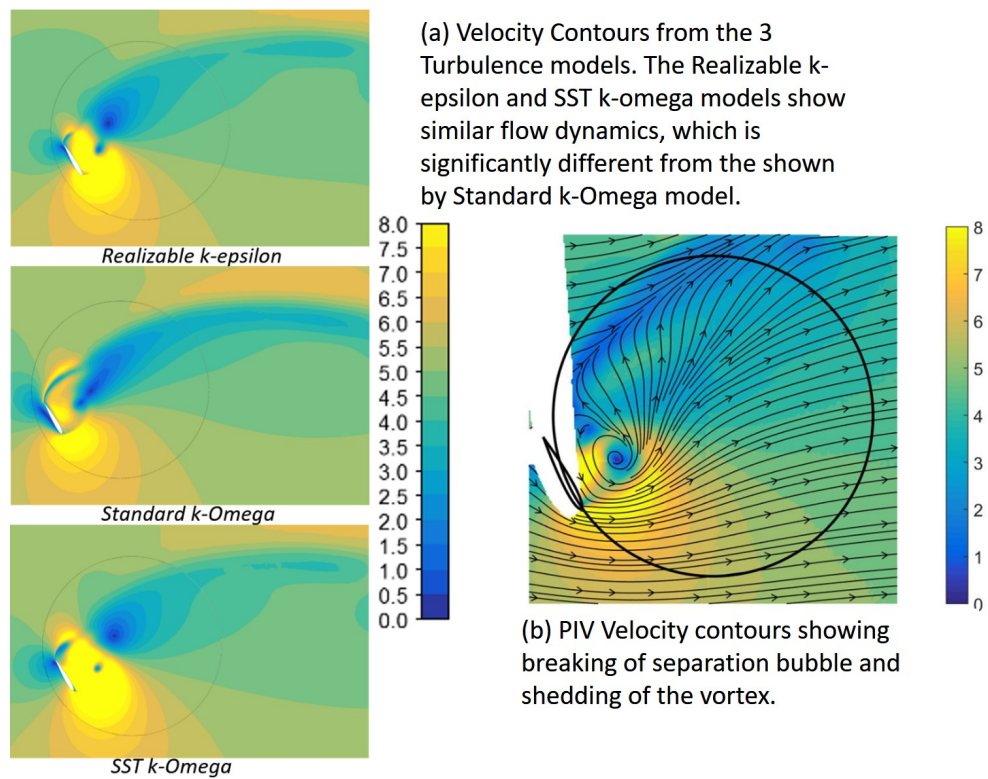
Figure 5.20: Comparison between different models and PIV data at 120 degree $\mu = 1.25$

(a) Velocity Contours from 3 Turbulence models. K-omega model predicts the flow more accurately in Unsteady region.

Realizable k-epsilon

Standard k-Omega

SST k-Omega

(b) PIV Velocity contour showing convection of vortex and high-velocity region.
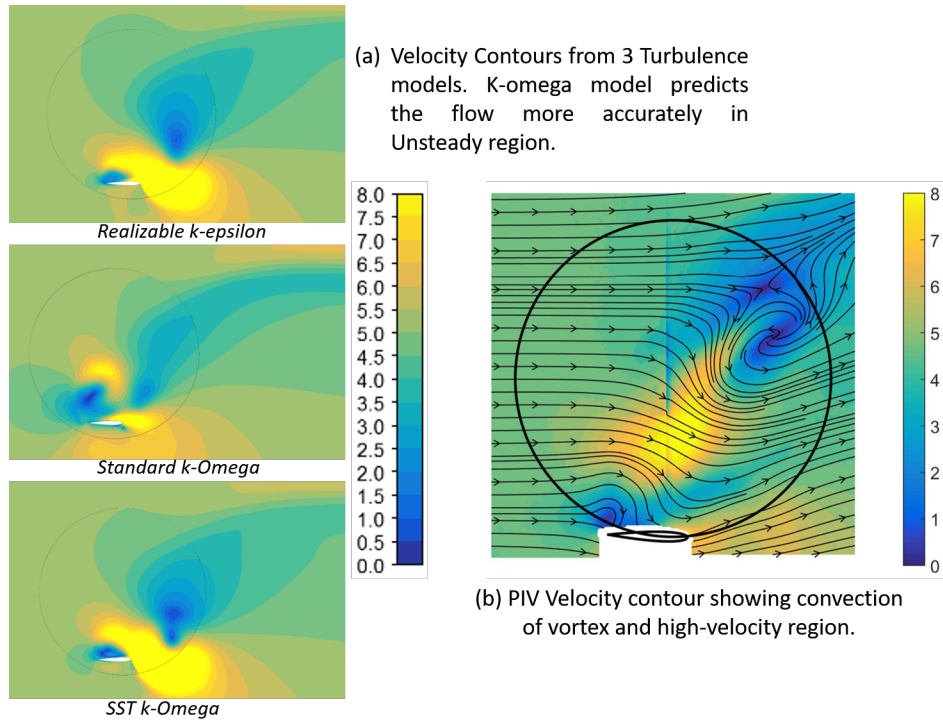
Figure 5.21: Comparison between different models and PIV data at 180 degree $\mu = 1.25$

$\mu = 0.75$

$\mu = 1$

$\mu = 1.25$

$\mu = 0.75$

$\mu = 1$

$\mu = 1.25$

$\mu = 0.75$

$\mu = 1$

$\mu = 1.25$

(a) CFD: Velocity Contours for three advance ratios at 90° azimuth angle.

(b) CFD: Vorticity Contours showing LEV and TEV in different phases for three advance ratios at 90° azimuth angle.

(c) PIV: Velocity Contours for three advance ratios.
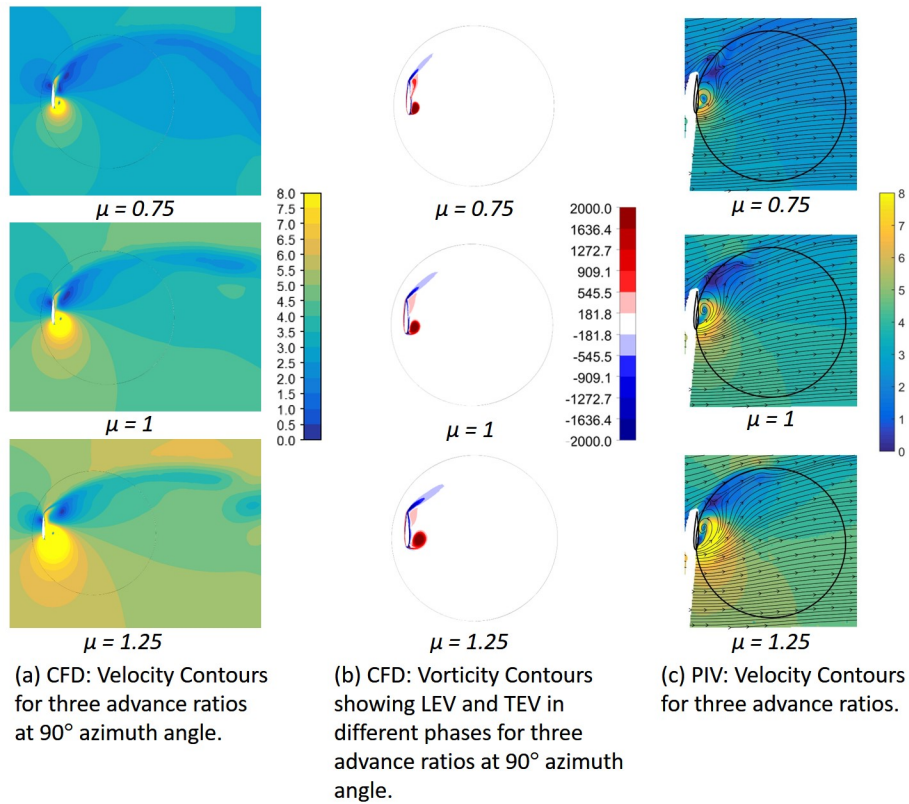
Figure 5.22: Contour plots comparing results from SST model and PIV at 90 degrees at different μ
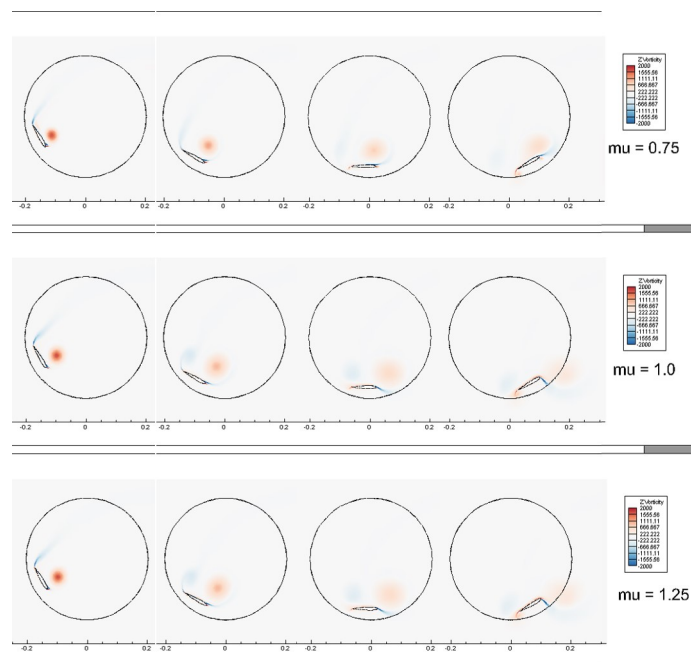
Figure 5.23: Vorticity from SST model as the airfoil rotates from 90-210 degrees at different μ

blade azimuth positions for $\mu = 0.75$, 1, and 1.25, respectively. It can be seen that the characteristic "U" shaped geometry of the wake formed inside the rotor (shown at $\theta = 180°$) is apparent at $mu = 0.75$ which leads to the blade-wake interaction. However, for $mu = 1$ and 1.25 this shape is not formed due to faster advection of the wake under the influence of higher free stream velocities which prevents the blade-wake interaction.
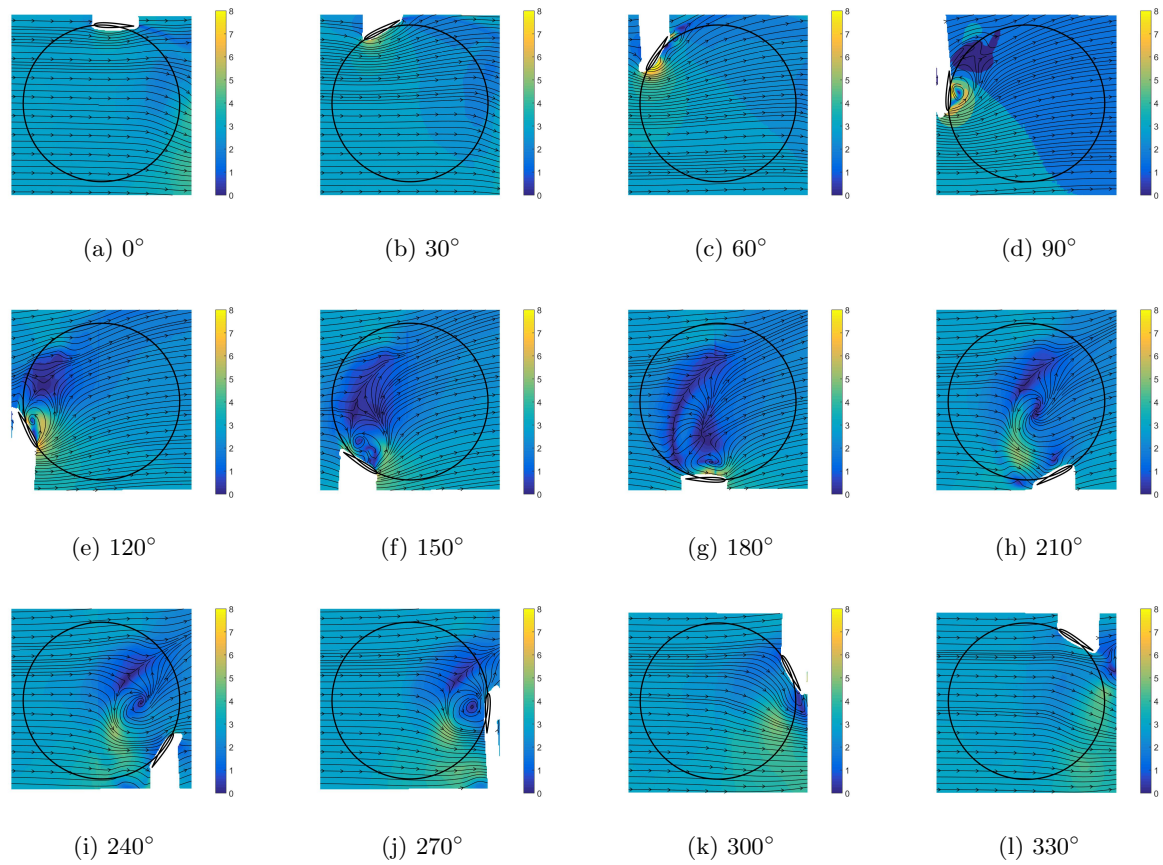
Figure 5.24: Velocity contours at 12 different instances showing the cycloidal rotor flow dynamics, 30 degrees phase apart for μ=0.75

(a) 0° (b) 30° (c) 60° (d) 90°

(e) 120° (f) 150° (g) 180° (h) 210°

(i) 240° (j) 270° (k) 300° (l) 330°
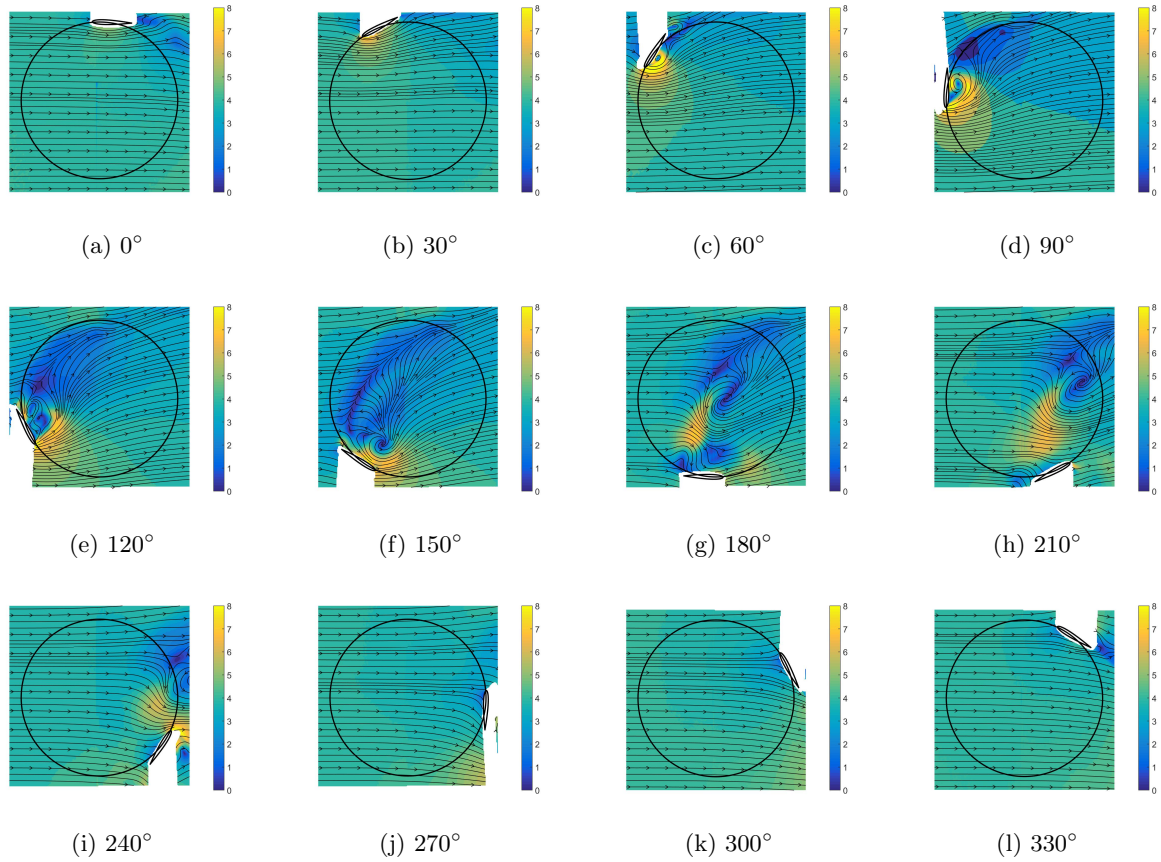
Figure 5.25: Velocity contours at 12 different instances showing the cycloidal rotor flow dynamics, 30 degrees phase apart for $\mu=1$

(a) 0°

(b) 30°

(c) 60°

(d) 90°

(e) 120°

(f) 150°

(g) 180°

(h) 210°

(i) 240°

(j) 270°

(k) 300°

(l) 330°

Figure 5.26: Velocity contours at 12 different instances showing the cycloidal rotor flow dynamics, 30 degrees phase apart for μ=1.25

Chapter 6

Conclusions

The flow dynamics of a cycloidal rotor system was studied as it translates through the advance ratios about $\mu = 1$. Experimentally results using PIV measurements were compared to the URANS and LES CFD results. Three cases were considered at advance ratios of $\mu = 0.75$, 1, and 1.25. Note, The free stream veloci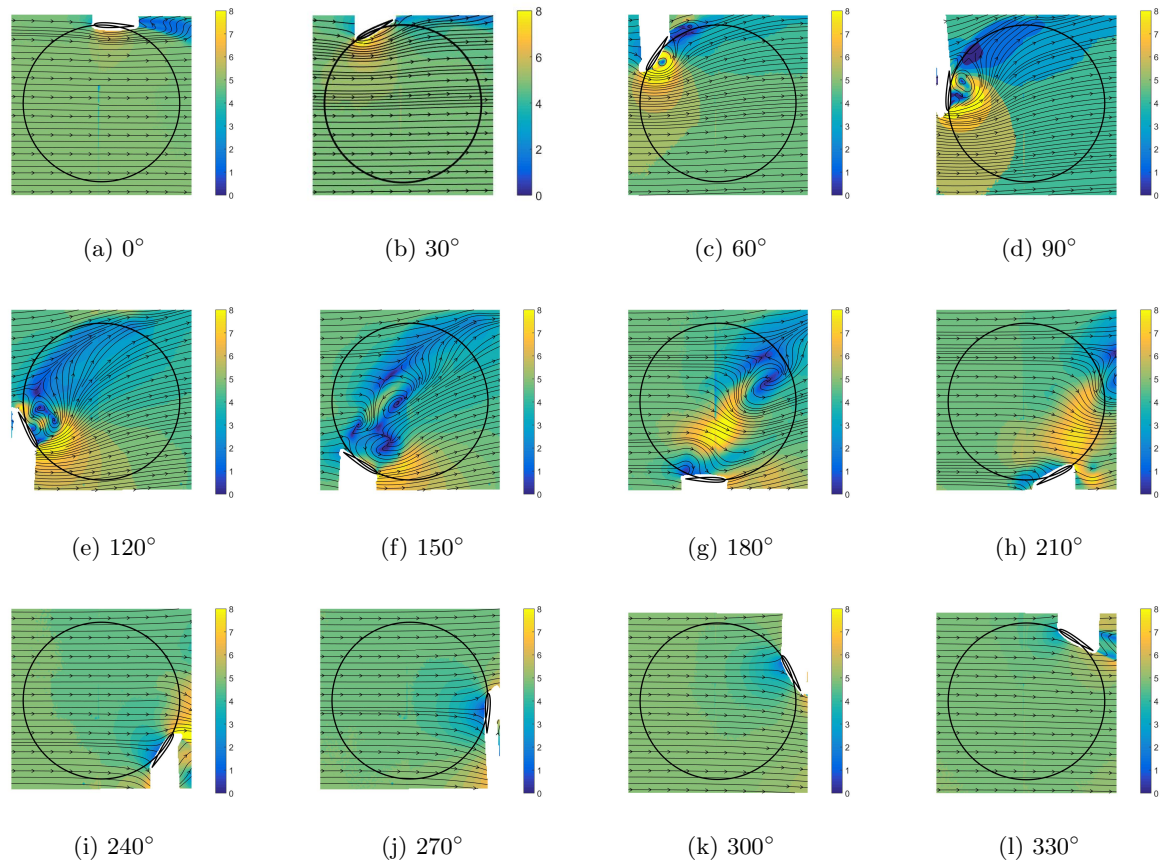ty and rotational speed were varied to obtain these three advance ratios. The results helped to elucidate the fundamental understanding of the unsteady aerodynamics of the system, with the major conclusions summarize below.

(1) The cycloidal rotor system operates at highly varying flow conditions throughout its rotation. The flow translates from high Reynolds number steady flow to low Reynolds number unsteady flow in every single rotation resulting in complex flow structures and dynamics. The combination of the change in local angle of attack and local resultant velocity results in varying force production. This is also responsible for the production of net force even when the airfoil is mounted a fixed geometric angle of attack of $\alpha = 0°$ (i.e the chord is perpendicular to the rotor radius).

(2) The flow dynamics can be generally divided into four sections - (1) the windward section ($315° < \theta < 45°$): the airfoil encounters the maximum flow velocity at minimum angle of attack, (2) upwind section ($45° < \theta < 135°$): the airfoil undergoes dynamic stall, (3) leeward section ($135° < \theta < 225°$): the airfoil sheds the vortex pair as it approaches minimum local velocity with highly unsteady flow, (4) downwind section ($225° < \theta < 315°$): the airfoil interacts with its own wakes and vortices.

(3) Eleven combinations of free stream and rotational velocities were studied to find velocity at the exit

of the rotor. Results confirm that the flow is similar for the same advance ratios and are independent of the flow Reynolds number.

(4) The occurrence of dynamic stall occurs at slightly different phase angles in all three advance ratios, but the phenomenon fundamentally remains the same with the apparent curling of the shear layer at the leading edge of the airfoil. This leads to the formation of a separation bubble at the airfoil surface. This occurs between $30° < \theta < 60°$ for every case. The Leading Edge Vortex (LEV) travels along the chord of the airfoil and separates from it at the trailing edge. However, even after separation, the LEV is dragged near the surface of the airfoil and finally moves away from its influence at the point to flow reversal on the airfoil.

(5) The dragging of LEV and wake shed from the trailing edge along with the airfoil is apparent in all cases. The wake is stretched under the influence of free stream and dragging by the airfoil.

(6) As the LEV is dragged near the airfoil surface it creates a region of high-velocity in the flow with affects the flow dynamics of the system.

(7) The trajectory followed by the LEV and wake from the trailing edge is very similar in all three cases, but the speed of advection across the rotor is different. Also the amount of curvature observed in the trajectories is different. The vortex interacts with the airfoil at $\theta = 270°$ for $\mu = 0.75$, and leaves the rotor at higher azimuth locations for $\mu = 1$ and 1.25 without interacting with the airfoil. The combined effect of the advection velocity and trajectory curvature decides the possibility and location of airfoil-vortex interaction.

(8) The advection of high-velocity region from the LEV and its interaction with the airfoil at different locations and intensities should affect the net force generation of the system. This local change in velocity around the airfoil also affects the strength of vortex generated at $\theta = 270°$.

(9) When comparing velocity contour of each case, it is seen that the flow for $\mu = 0.75$ at an $\theta = 0°$ is very similar to the flow at $\theta = 30°$ for $\mu = 1.25$ in the upwind section. In the downwind section the phase lag stretches from $\Delta\theta = 30°$ to $\Delta\theta = 60°$.

(10) A CFD study was conducted to compare the general flow dynamics simulated to those seen in the PIV results, and to get an idea of the forces produced by the system. None of the CFD results obtained from this analysis matched the PIV results completely. However, a tertiary comparison of turbulence models with the PIV results shows a difference in performance of each of the model at different flow conditions. The realizable k-ϵ model and SST k-ω model show good prediction of dynamic stall, but the standard k-ω model predicts the flow near the airfoil more accurately in the unsteady region.

(11) Although, the CFD results could not predict the complex flow dynamics like the traveling of LEV on the blade chord, it was however, able to show some basic characteristics of dynamic stall, blade-vortex interaction, etc. The force coefficients show that the difference in peaks of the cyclically changing drag and lift curves decrease as the advance ratio increases. The system produces more lift force for $\mu = 0.75$ as compared to $\mu = 1.25$, but also produce more drag force. The results also show a quick dissipation of vortex energy as the airfoil rotates from $\theta = 90°$ to $\theta = 210°$. However, this analysis in no way represents the true unsteady character of the cycloidal rotor flow dynamics.

(12) The characteristic "U" shaped geometry of the wake formed inside the rotor (shown at $\theta = 180°$) is apparent at $\mu = 0.75$ which leads to the blade-wake interaction. However, for $\mu = 1$ and 1.25 this shape is not formed due to faster advection of the wake under the influence of higher free stream velocities which prevents the blade-wake interaction.

Chapter 7

Future Recommendations

The present study was focused on understanding the basic unsteady aerodynamics of a cycloidal rotor system at different advance ratios. For future experiments, it is recommended to further extend the range of downstream flow. For the flow inside the rotor, more azimuth positions should be captured in the experimental data. This can be done by finding interesting points using CFD simulations and focusing the experiments at those phase angles. The experimental setup should ideally be expanded to capture the flow in the laser shadow region so that the resultant forces can be experimentally predicted from the circulation around the airfoil at every instance. More experiments should be run at different instantaneous angles of attack. Also, to evaluate the difference in flow dynamics with the change in chord-radius ratio and fixed point location for simple fixed airfoil system. As it is seen that the phenomenon of blade-vortex interaction is not a universal one, a quantitative method should be developed to help predict this behavior and hence finding the best operating conditions for the system. Since the turbulence models behave differently as the flow conditions change, a combination of methods or improved mesh resolution and carefully chosen parameters must be used to get accurate results.

Bibliography

[1] Design and development of an unconventional VTOL micro air vehicle: The Cyclocopter, volume 8373, 2012.

[2] Zachary Adams and Casey Fagley. Novel cyclorotor pitching mechanism for operation at curtate and prolate advance ratios. In AIAA Paper 2013-0501, 2013.

[3] Autodesk. Autodesk knowledge network: Sst k-omega turbulence models. Website, 2014.

[4] Moble Benedict. FUNDAMENTAL UNDERSTANDING OF THE CYCLOIDAL-ROTOR CONCEPT FOR MICRO AIR VEHICLE APPLICATIONS. PhD thesis, University of Maryland, College Park, 2010.

[5] Moble Benedict, Tejaswi Jarugumilli, and Inderjit Chopra. Effect of rotor geometry and blade kinematics on cycloidal rotor hover performance. Journal of Aircraft, Vol. 50, No. 5, 2013.

[6] Moble Benedict, Tejaswi Jarugumilli, Vinod Lakshminarayan, and Inderjit Chopra. Effect of flow curvature on forward flight performance of a micro-air-vehicle-scale cycloidal-rotor. AIAA Journal, Vol. 52, No. 6, 2014.

[7] Moble Benedict, Manikandan Ramasamy, and Inderjit Chopra. Improving the aerodynamic performance of micro-air-vehiclescale cycloidal rotor: An experimental approach. JOURNAL OF AIRCRAFT Vol. 47, No. 4, 2010.

[8] Moblie Benedict. Performance of a cycloidal rotor concept for micro air vehicle applications. JOURNAL OF THE AMERICAN HELICOPTER SOCIETY, 55(022002), 2010.

[9] Eric Besnard, Adeline Schmitz, George Tzong, Kalle Kaups, and Hamid Hefazi. Hydrofoil design and optimization for fast ships. Proceedings of the 1998 ASME International Congress and Exhibition, 1998.

[10] C.G Boirum and S.L. Post. Review of historic and modern cyclogyro design. In AIAA 2009-5023, Denver, CO, 2009. 45th AIAA/ASME/SAE/ASEE, Joint Propulsion Conference and Exhibit.

[11] James. H. Boschma. Modern aviation applications for cycloidal propulsion. In 1st AIAA, Aircraft, Technology Integration, and Operations Forum, Aviation Technology, Integration, and Operations (ATIO) Conferences, 2001.

[12] D. Castelein. Dynamic stall on vertical axis wind turbines. Master's thesis, European Wind Energy Master - EWEM, 2015.

[13] C.B.Strandgren. The theory of the strandgren cyclogiro. Technical report, National Advisory Committee for Aeronautics, 1933.

[14] Casey P. Fagley, Christopher O. Porter, and Thomas E. McLaughlin. Curvature effects of a cycloidally rotating airfoil. In 52nd Aerospace Sciences Meeting, AIAA SciTech Forum, 2014.

[15] C. J. Simao Ferreira, A. van Zuijlen, H. Bijl, G. van Bussel, and G. van Kuik. Simulating dynamic stall in a two-dimensional vertical-axis wind turbine: verification and validation with particle image velocimetry data. Wind Energy, 2010.

[16] Carlos Simao Ferreira. The near wake of the VAWT. PhD thesis, TU Delft, 2009.

[17] I E Garrick. Propulsion of a flapping and oscillating airfoil. Technical report, National Advisory Committee for Aeronautics, Langley Aeronautical Lab, 1937.

[18] Kobra Gharali and David A. Johnson. Dynamic stall simulation of a pitching airfoil under unsteady freestream velocity. Journal of Fluids and Structures, Volume 42, 2013.

[19] T Gocmen. Wind turbine wake models developed at the technical University of Denmark: A review. PhD thesis, University of Denmark, 2016.

[20] Tuhfe Gocmen, Paul van der Laan, Pierre-Elouan Rethore, Alfredo Pena Diaz, Gunner Chr. Larsen, and Soren Ott. Wind turbine wake models developed at the technical university of denmark: A review. Renewable and Sustainable Energy Reviews, 60, 2016.

[21] Ulgen Gulcat. Fundamentals of modern unsteady aerodynamics. Springer, 2010.

[22] In Seong Hwang, Seung Yong Min, Choong Hee Lee, and Seung Jo Kim. Development of a four-rotor cyclocopter. JOURNAL OF AIRCRAFT, 2008.

[23] G. Iosilevskii. Aerodynamics of the cyclogiro. In 33rd AIAA Fluid Dynamics Conference and Exhibit, Fluid Dynamics, 2003.

[24] Tejaswi Jarugumilli. An experimental investigation of a micro air vehicle-scale cycloidal rotor in forward flight. Master's thesis, University of Maryland, College Park, 2010.

[25] Seung Jo Kim, Chul Yong Yun, Daesung Kim, Youngha Yoon, and Illkyung Park. Design and performance tests of cycloidal propulsion systems. In 44th AIAA/ASME/ASCE/AHS/ASC Structures, Structural Dynamics, and Materials Conference, 2003.

[26] F. K. Kirsten. Cycloidal propulsion applied to aircraft. Transactions of the American Society of Mechanical Engineers, 50(12), 1928.

[27] J. Leger, J. Pascoa, and C. Xisto. 3d effects in cyclorotor propulsion systems. In International Mechanical Engineering Congress and Exposition IMECE2015, November 2015.

[28] Osama A. Marzouk and E. David Huckaby. Simulation of a swirling gas-particle flow using different k-epsilon models and particle-parcel relationships. Engineering Letters, 18(1), 2010.

[29] Michael Lynn McNabb. Development of a cycloidal propulsion computer model and comparison with experiment. Master's thesis, Mississippi State University, 2001.

[30] PG Migliore, W. P. Wolfe, and J. B. Fanucci. Flow curvature effects on darrius turbine blade aerodynamics. Journal of Energy, Vol. 4, No. 2, 1980.

[31] B. Nagler. Improvements in flyingmachines employing rotating wing systems. U.K. Patent No. 280,849, 1926.

[32] Eric Parsons. Investigation and characterization of a cycloidal rotor for application to a micro-air vehicle. Master's thesis, University of Maryland, College Park, 2005.

[33] Jose C. Pascoa and Galina I. Ilieva. Overcoming stopovers in cycloidal rotor propulsion integration on air vehicles. In ASME 2012 International Design Engineering Technical Conferences and Computers and Information in Engineering Conference Volume 6: 1st Biennial International Conference on Dynamics for Design; 14th International Conference on Advanced Vehicle Technologies, 2012.

[34] Christopher Rumsey. Nasa langley research center turbulence modeling resource. Website, June 2015.

[35] H. Sachse. Kristen-boeing propeller. Technical report, National Advisory committee for aeronautics; Technical Memorandum No. 351., 1926.

[36] Stefan Siegel, Jurgen Seidel, Kelly Cohen, and Thomas McLaughlin. A cycloidal propeller using dynamic lift. In 37th AIAA Fluid Dynamics Conference and Exhibit, 2007.

[37] Jayant Sirohi, Eric Parsons, and Inderjit Chopra. Hover performance of a cycloidal rotor for a micro air vehicle. Journal of the American Helicopter Society, 2007.

[38] Jiwei Tang, Yu Hu, and Bifeng Song. Investigation on the unsteady aerodynamics of cycloidal propeller in hovering flight. Proceedings of the Institution of Mechanical Engineers: Journal of Aerospace Engineering, 2015.

[39] Hsieh-Chen Tsai and Tim Coloniusy. Coriolis effect on dynamic stall in a vertical axis wind turbine at moderate reynolds number. In AIAA Aviation, 32nd AIAA Applied Aerodynamics Conference, 2012.

[40] Various. Cycloidal rotor optimized for propulsion. Website, December 2014.

[41] Heidenheim Voith AG. Voith schneider. Wikipedia, 2007.

[42] Shengyi Wang, Derek B. Ingham, Lin Ma, Mohamed Pourkashanian, and Zhi Tao. Numerical investigations on dynamic stall of low reynolds number flow around oscillating airfoils. Computers and Fluids, 39(9):15291541, October 2010.

[43] J. Wheatley. Simplified aerodynamic analysis of the cyclogiro rotating wing system. Technical report, National Advisory Committee for Aeronautics. Langley Aeronautical Lab, 1930.

[44] C. M. Xisto. Parametric analysis of a large-scale cycloidal rotor in hovering conditions. J. Aerosp. Eng. , 10.1061/(ASCE)AS.1943-5525.0000658 , 04016066, 2016.

[45] Carlos M. Xisto, Jose C. Pascoa, Jakson A. Leger, Pierangelo Masarati, Giuseppe Quaranta, Marco Morandini, and Louis Gagnon. Numerical modelling of geometrical effects in the performance of a cycloidal rotor. In 11th World Congress on Computational Mechanics (WCCM XI), 2014.

[46] K. Yang. Aerodynamic analysis of an mavscale cycloidal rotor system using a structured overset rans solver. Master's thesis, University of Maryland at College Park, 2010.

[47] Hu Yu, Lim Kah Bin, and Tay Wee Beng. The investigation of cyclogyro design and the performance. In 25th Congress of International Council of the Aeronautical Sciences, 2006.

[48] Chul Yong Yun and Illkyung Park. A new vtol uav cyclocopter with cycloidal blades system. In American Helicopter Society; 60th annual forum proceedings, 2004.